https://doi.org/10.5194/essd-2025-593
Preprint. Discussion started: 7 October 2025

Open Access Earth System Science Data Discussions

A Global Black Carbon Dataset of Column Concentration and Microphysical Information Derived from MISR Multi-band Observations and Mie Scattering Simulations

Zhewen Liu[1], Jason Blake Cohen[1*], Pravash Tiwari[1], Luoyao Guan[1], Shuo Wang[1], Kai Qin[1]

[1]School of Environment Science and Spatial Informatics, China University of Mining and Technology, Xuzhou, 221116, China

Correspondence to: Jason Blake Cohen (jasonbc@alum.mit.edu; jasonbc@cumt.edu.cn)

Abstract.

Black carbon, a major absorbing component of atmospheric aerosols, plays an important role in climate regulation, air quality, and human health, yet its column concentration and microphysical properties at regional and global scales remains highly uncertain. In this study, we implement an integrated approach that combines multi-angle, multi-band observations from the Multi-angle Imaging SpectroRadiometer with a Mie scattering framework to estimate black carbon column properties including size and mixing state globally on a daily basis. By constraining particle size distributions with absorption aerosol optical depth and single scattering albedo across all four bands, the method simultaneously retrieves number and mass concentrations. Long-term simulations from 2005 to 2020 reveal distinct spatial and temporal patterns, with particularly high levels over biomass burning regions in Africa and South America as well as industrial and urban centers in Asia. Comparisons with ground-based sun photometer measurements and reanalysis data confirm the robustness and accuracy of the estimates. The resulting dataset provides a consistent global record of black carbon column concentrations, offering valuable support for constraining climate models, improving assessments of aerosol radiative forcing, and informing targeted mitigation strategies.

1 Introduction

Atmospheric aerosols, a mixture of fine solid and liquid particles widely distributed within the troposphere, play a pivotal role in climate systems, air quality, and human health due to their complex sources and heterogeneous distribution. Among these, black carbon (BC), characterized by its unique optical and physicochemical properties (Hodnebrog et al., 2014; Lund et al., 2018), has garnered increasing attention in atmospheric science (Jacobson, 2001; Li et al., 2016). BC's strong solar radiation absorption capacity makes it among the most critical climate forcing agents after carbon dioxide, with profound implications for global warming and regional climate change (Ramanathan and Carmichael, 2008; Li et al., 2022a). Predominantly generated through the incomplete combustion of carbonaceous materials (Bond et al., 2013; Xie et al., 2025), BC sources include natural events (Cohen, 2014), such as volcanic eruptions and wildfires, and anthropogenic activities

https://doi.org/10.5194/essd-2025-593
Preprint. Discussion started: 7 October 2025

(Szidat et al., 2006; Lin et al., 2020; Wang et al., 2020), such as fossil fuel combustion, industrial sources, steel and other materials production, and vehicular emissions. Freshly emitted BC particles are typically independent entities (Tanaka et al., 2012), but aging processes in the atmosphere lead to interactions with other primary aerosols, secondary aerosol vapors, and atmospheric water vapor, forming a "core-shell" type of structure that is thermodynamically stable (Chen et al., 2013; Wang et al., 2021b). This aged aerosol is the dominant type found in the in-situ environment (Roberts and Jones, 2004; Mylläri et al., 2019) especially so in more heavily polluted areas (He et al., 2015). Such a configuration amplifies BC's light absorption capabilities (Hansen et al., 2007; Chung et al., 2012; Cappa et al., 2012; Tiwari et al., 2023), further intensifying its impact on radiative balance and atmospheric dynamics, especially regionally (Lund et al., 2017; Wang et al., 2019).

Additionally, BC deposition on snow and ice surfaces reduces albedo (Zhao and Garrett, 2015; Zhao et al., 2023), accelerating melt rates and exerting a significant influence on the climate, particularly in high-latitude and high-altitude regions. Beyond its climatic impacts (Rosenfeld et al., 2014; Ding et al., 2016; Ma et al., 2020), BC disrupts boundary layer structures, facilitates haze formation, and inhibits pollutant dispersion, thereby degrading air quality (Guo et al., 2019). Furthermore, BC particles carry toxic combustion byproducts, posing relatively more severe health risks than $PM_{2.5}$ on average, including increased respiratory and cardiovascular disease incidences (Cassee et al., 2013; Yang et al., 2021), representing a significant public health concern. Therefore, enhancing BC monitoring and research is essential for quantifying its sources, evolution, and impacts, improving climate model predictions, and formulating targeted pollution mitigation and emission reduction strategies.

The column concentration of BC, an essential indicator of its total amount in the atmospheric column, has been widely used to evaluate BC's radiative effects and climate impact. Advances in ground-based observation, satellite remote sensing, and numerical simulations have significantly enriched the understanding of its spatiotemporal distribution and environmental consequences (Liu et al., 2024a, b; Tiwari et al., 2025). Ground-based measurements using instruments such as sun photometers, BC analyzers, and aerosol optical property devices provide high temporal resolution and measurement accuracy but are spatially confined to specific regions (Schwarz et al., 2008; Lee et al., 2016). Seasonal variations in BC column concentrations are evident (Li et al., 2023; Yu et al., 2024), with studies in high-pollution areas indicating substantially higher levels during winter compared to summer, or during intense periods of industrial activity and/or local biomass burning. However, the limited spatial coverage of ground observations fails to comprehensively represent global BC column concentration distributions.

Satellite remote sensing has opened new avenues for monitoring BC column concentrations at regional and global scales (Yu et al., 2024). Traditional approaches have used retrievals of aerosol optical depth from satellite observations to derive BC column mass concentrations using fixed and/or simplified microphysical properties of BC (Li et al., 2019; Torres et al., 2020; Li et al., 2020; Junghenn Noyes et al., 2022; Limbacher et al., 2022; Li et al., 2022b; Zhang et al., 2024). However, challenges in spatial resolution and data accuracy persist, especially in regions with complex terrain, severe pollution, where the sources of BC emissions are undergoing rapid changes, where different sources of pollutants mix with each other, or in other locations where retrieval reliability and uncertainty requires further improvement (Wang et al., 2021c; Lu et al., 2025).

https://doi.org/10.5194/essd-2025-593
Preprint. Discussion started: 7 October 2025

Numerical simulations have proven invaluable in investigating the sources, transport, and deposition processes of BC column concentrations (Randles et al., 2017; Bousserez et al., 2020; Wang et al., 2021a). Atmospheric chemical transport models and climate models reveal that long-range BC transport contributes significantly to high concentrations in certain regions and exerts substantial downstream climatic and environmental impacts (Wang et al., 2017; Tegtmeier et al., 2022; Yang et al., 2022; Senf et al., 2023; Zhao et al., 2024; Chakraborty et al., 2025). Despite their spatial and temporal comprehensiveness, the accuracy of numerical simulations heavily depends on emission inventories in both space and time (Wang et al., 2025; Li et al., 2025), in addition to the understanding and parameterization of, as well as access to sufficient data to compute relevant physicochemical processes (Chen and Prinn, 2006; Kim et al., 2008).

This study proposes an innovative methodology for estimating BC column concentrations by integrating satellite remote sensing data, aiming to enhance calculation efficiency and accuracy through the effective utilization of multisource satellite datasets. Specifically, the method involves leveraging data from four spectral bands of the MISR satellite for daily preprocessing to obtain critical parameters, including Absorption Aerosol Optical Depth (AAOD) and Single Scattering Albedo (SSA). These parameters are then input into the Mie scattering model (MIE model) for particulate size retrieval, followed by BC column concentration estimation. This estimation encompasses both mass and particle count data, providing a comprehensive basis for evaluating BC's environmental and climatic effects. Detailed sensitivity analyses of the data were conducted to ensure result reliability and stability. Furthermore, comparisons with AERONET sunphotometer data and MERRA-2 reanalysis validate and demonstrate the method's accuracy, realism over areas with little a priori data, and applicability over global and decadal scales. This integrated approach, combining satellite remote sensing and model computations, presents an innovative solution for BC column concentration estimation, improving data processing efficiency and mitigating the limitations of traditional single-source methods. By effectively leveraging multi-band satellite observations, this methodology holds promise for advancing aerosol monitoring and climate model validation, offering robust technical support for regional and global BC research.

2 Materials and methods

2.1 MISR AOD/SSA/AAOD

The Multi-angle Imaging Spectro Radiometer (MISR), a key component of NASA’s Earth Observing System (EOS), captures multi-angle reflected sunlight images to investigate Earth's ecosystems and climate change. Launched aboard the EOS AM-1 satellite in 1998, MISR consists of nine push-broom cameras that image Earth in four spectral bands (blue, green, red, and near-infrared) and provide global coverage every nine days. Multi-angle observations mitigate the influence of vertical aerosol distribution heterogeneity on aerosol optical depth (AOD) retrievals and aid in distinguishing optical properties of various aerosol types based on their sphericity.

The product used in this study, MIL3DAEN_4, is MISR’s Level 3 global aerosol product (CGAS), providing aerosol information on a global 0.5° × 0.5° latitude-longitude grid. These data are aggregated from higher-resolution (4.4 km × 4.4

https://doi.org/10.5194/essd-2025-593
Preprint. Discussion started: 7 October 2025

km) MISR Level 2 aerosol retrievals and include daily, monthly, seasonal, and annual averages. MIL3DAEN_4 is generated through rigorous MISR data processing steps to ensure product accuracy and scientific validity.

A key feature of the MIL3DAEN_4 product is its capacity for global-scale aerosol monitoring and multi-temporal data aggregation. By utilizing multi-angle imaging, it provides aerosol optical depth (AOD) and absorption aerosol optical depth (AAOD) data, effectively capturing both scattering and absorbing properties of aerosols. Specifically, the single scattering albedo (SSA) metric within MIL3DAEN_4 analyzes aerosol scattering and absorbing capacities. SSA, calculated from AOD and AAOD data, approaches 1 for highly scattering aerosols, while lower SSA values indicate stronger absorption. This metric is crucial for classifying aerosols and studying their physical properties, enabling differentiation between absorbing and non-absorbing aerosols based on their optical characteristics.

In MIL3DAEN_4, the gridded data resolution is 0.5° × 0.5°, with each grid cell value averaged from higher-resolution Level 2 product samples, assigning equal weight without regard to sampling frequency. All quality-controlled samples within a grid are used to compute mean values, ensuring product representativeness and reliability. To maintain data credibility, the MIL3DAEN_4 product excludes samples failing quality checks, such as low-quality aerosol retrievals from regions like Greenland and Antarctica.

Moreover, MIL3DAEN_4 offers substantial temporal and spatial coverage, supporting analyses of aerosol temporal trends and spatial distributions. Accumulating long-term data, MIL3DAEN_4 facilitates examination of aerosols' long-term trends and their potential impacts on climate and ecosystems. Despite its relatively coarse spatial resolution, MIL3DAEN_4 provides unique insights into aerosols' role within the Earth's climate system on both global and regional scales. Compared with other aerosol remote sensing products, MISR's multi-angle approach enables improved retrieval accuracy of aerosol optical properties, particularly for specific regions and aerosol types.

In summary, the MIL3DAEN_4 product, as MISR's Level 3 aerosol product, aggregates aerosol optical and physical characteristics in a globally gridded format, offering multi-temporal data on aerosol variations with significant scientific value. MIL3DAEN_4 plays a critical role in studies of aerosol scattering and absorption characteristics. Although limited by its spatial resolution, its multi-angle and multi-spectral observational capability provides robust data for monitoring aerosols at varying spatial and temporal scales.

2.2 MIE model

The Mie model is a theoretical model used to calculate the interaction between electromagnetic waves and spherical particles and holds significant applications in aerosol optical property research. Named after the German physicist Gustav Mie, the Mie scattering model is based on Maxwell's equations and addresses the scattering and absorption of incident electromagnetic waves by spherical particles to determine properties such as the intensity, phase, and polarization of scattered light. This model considers factors such as the wavelength of incident radiation, particle size (expressed through the size parameter x, where $x = \pi D / \lambda$, with D as particle diameter and λ as wavelength), and the particle's complex refractive index ($m = n + ik$, where n is the real part and k is the imaginary part of the refractive index).

https://doi.org/10.5194/essd-2025-593
Preprint. Discussion started: 7 October 2025

Using a "core-shell" aerosol structure, the Mie scattering optical model is applied to calculate radiative parameters for extinction aerosols. This model, based on Mie scattering theory, treats light waves as electron waves and solves Maxwell's equations for both internal and external regions of the particle under boundary conditions determined by particle shape and size. Mie scattering theory thus provides an exact solution for a homogeneous, spherical particle in the far-field under monochromatic plane wave illumination. For example, with known particle chemical composition and size, the model can compute scattering coefficients, absorption coefficients, extinction coefficients, and asymmetry factors.

For a single spherical particle of radius r and complex refractive index mmm, illuminated by light of wavelength λ, the calculation formula for the Mie scattering coefficient is as follows.

$$a = \frac{m^2 j_n(mx)[x j_n(x)]' - j_n(x)[mx j_n(mx)]'}{m^2 j_n(mx)\left[x h_n^{(1)}(x)\right]' - h_n^{(1)}(x)[mx j_n(mx)]'} \quad (1)$$

$$b = \frac{j_n(mx)[x j_n(x)]' - j_n(x)[mx j_n(mx)]'}{j_n(mx)\left[x h_n^{(1)}(x)\right]' - h_n^{(1)}(x)[mx j_n(mx)]'} \quad (2)$$

where

$$j_n(z) = \sqrt{\frac{\pi}{2z}} J_{n+0.5}(z) \quad (3)$$

$$y_n(z) = \sqrt{\frac{\pi}{2z}} Y_{n+0.5}(z) \quad (4)$$

$$h_n(z) = j_n(z) + i y_n(z) \quad (5)$$

where J_n and Y_n are the first- and second-kind Bessel functions, respectively. The scattering efficiency of the particle is then given by:

$$Q_{sca} = \frac{2}{x^2} \sum_{x^2}^{\infty} (2n+1)(|a_n|^2 + |b_n|^2) \quad (6)$$

The extinction efficiency is:

$$Q_{ext} = \frac{2}{x^2} \sum_{n=1}^{\infty} (2n+1) Re(a_n + b_n) \quad (7)$$

$$Q_{abs} = Q_{ext} - Q_{sca} \quad (8)$$

https://doi.org/10.5194/essd-2025-593
Preprint. Discussion started: 7 October 2025

3 Results

3.1 Utilizing MISR Data and Regional Division for Enhanced Black Carbon Analysis

To achieve more comprehensive coverage over a longer timeframe and reduce the uncertainty from integrating multiple data sources, this study utilizes remote sensing observations provided by MISR. Compared to other remote sensing sources, MISR not only offers a long-term observation record since 2000 but also provides multispectral data across four bands, which serves as an important foundation for more accurately calculating BC-related parameters. The multi-angle observation capability of MISR demonstrates exceptional performance in identifying aerosol optical properties, particularly in retrieving key parameters such as AAOD, where MISR data significantly enhances estimation accuracy.

For data selection, this study applied a threshold condition of AOD(443nm) > 0.25. This criterion reflects findings from previous studies showing that when AOD is relatively high, AAOD measurements become more reliable, thereby reducing observational uncertainty (Mallet et al., 2017; Schutgens et al., 2021; Zhang et al., 2025). Consequently, only the subset of MISR pixels from October 2004 to December 2020 meeting this criterion were selected. This filtering method enables the acquisition of more reliable BC data for analyzing its global distribution and spatiotemporal variation trends. For consistency in annual statistics and interannual trend analysis, we restricted the year-by-year evaluation to complete calendar years (2005–2020). This approach ensures comparability across years and avoids biases associated with partial-year data in 2004, although all individual days of data are retained in the complete dataset.

Considering the extensive observations spanning 16 years, this study adopted a global regional partitioning method based on Cohen and Wang (2014), as shown in Figure 1 (North America, South America, Europe, Africa, East Asia, Southeast Asia, South Asia, Nouth Asia, Oceania), to enhance computational and analytical efficiency. This method divides the globe into nine major regions, addressing both the global-scale analytical needs and adapting to the specific climate and geographic features of each region. Additionally, to further optimize research accuracy, adjustments were made for parts of Australia, Southeast Asia, and East Asia, considering the unique climate conditions and aerosol emission characteristics of these areas. This adjustment ensures more precise estimation of BC parameters in these critical regions.

Through this systematic regional division strategy, we can better utilize MISR data to analyze the spatiotemporal distribution patterns of BC across different regions. By leveraging MISR's long-term observational timeline, this study not only unveils trends in BC's spatiotemporal variations but also provides critical scientific evidence for climate modeling and environmental policy development.

https://doi.org/10.5194/essd-2025-593
Preprint. Discussion started: 7 October 2025

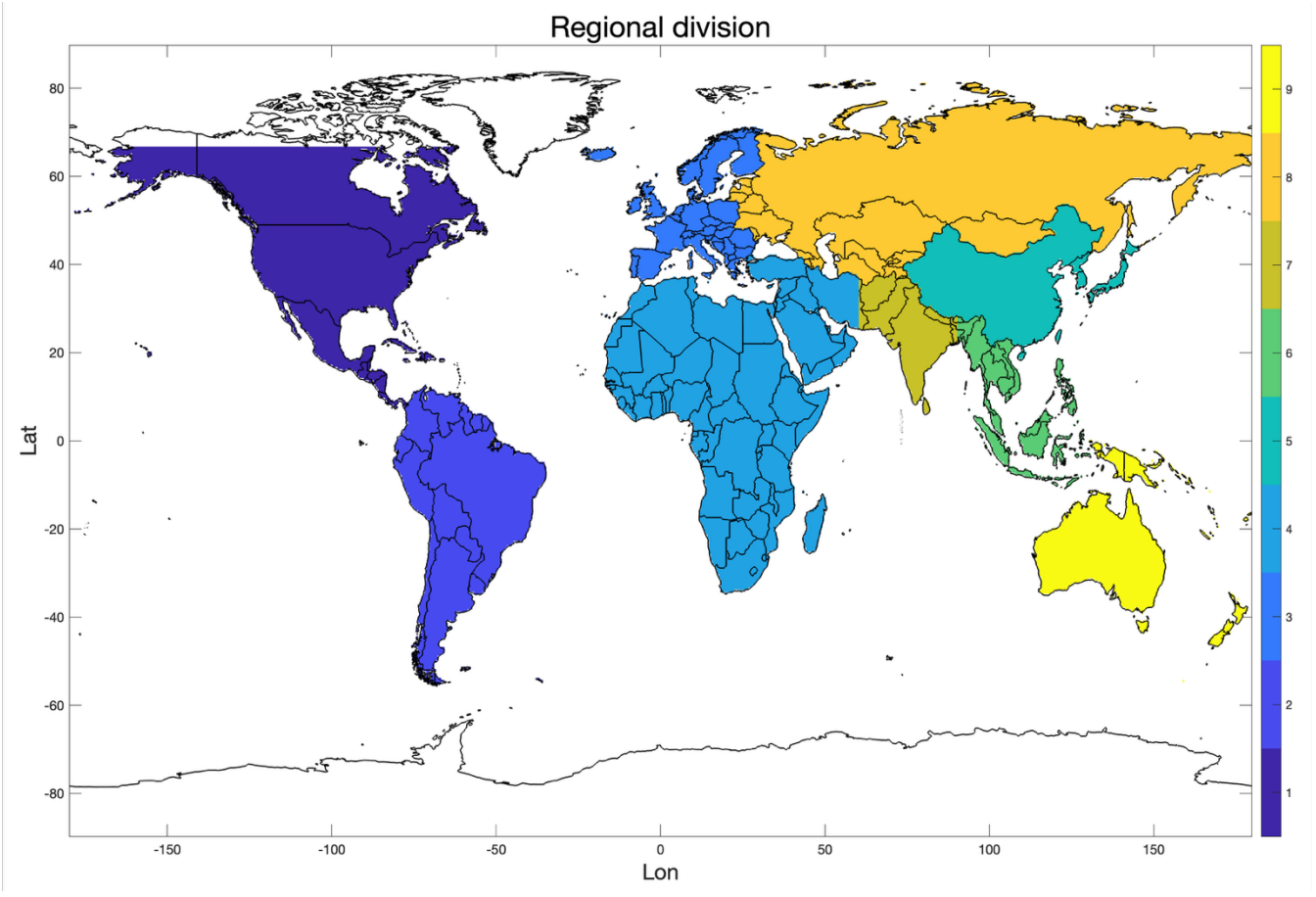

Figure 1. The nine geographic spatial defined regions used in this study.

3.2 Simulation of Aerosol Optical Properties Using SSA Constraints and Particle Size Combinations

To comprehensively assess the impact of different particle size combinations on aerosol optical properties, this study selects a "core" particle size range of 50–500 nm (in 10 nm increments) and a "shell" size range of 50–1000 nm (also in 10 nm increments). Utilizing this size range combination, we conducted a series of numerical simulations based on Mie scattering theory to analyze the scattering and absorption properties under various size distributions. This approach not only elucidates the changes in aerosol particles' optical properties across different wavelengths but also provides a scientific basis for understanding their environmental roles.

In particular, this study focuses on the SSA, a key parameter that describes the ratio of scattering to absorption, which is crucial for understanding the optical characteristics of particles. SSA values across different wavelengths were calculated and considered as constraints in the simulations, serving as essential boundary conditions for the model. These constraints allowed us to verify the validity of the simulation results, while SSA boundaries also provided reliable criteria for selecting final solutions, ensuring the data's authenticity and the model's scientific rigor.

https://doi.org/10.5194/essd-2025-593
Preprint. Discussion started: 7 October 2025

Open Access Earth System Science Data Discussions

In practice, we used SSA observations from MISR's four bands to constrain each spatial grid point on a daily basis. Observed values from each band, explicitly considering the ±0.03 uncertainty of SSA observations (Torres et al., 2020; Tiwari et al., 2025), defined a possible solution space, with only grid points that met the range requirements across all four bands being retained. This multi-band constraint analysis method enhances the reliability of the simulation results and avoids biases that may arise from single-band analyses. Through this filtering process, we obtained a set of particle radii that meet the observation criteria, representing the plausible particle size ranges under specific conditions and laying a foundation for further analysis of aerosol scattering and absorption properties.

The methodology developed in this study not only allows for precise simulation of aerosol optical properties across different size combinations but also provides a reference framework for future research. This particle size simulation approach will significantly support more comprehensive aerosol studies in environmental science, particularly in climate modeling and air pollution analysis. Additionally, by constraining the optical properties data across multiple wavelengths, our study enhances understanding of aerosol scattering and absorption behavior, particularly when analyzing environmental impacts, substantially improving the credibility and accuracy of the results. These findings offer new insights into the impact of aerosols on climate change and provide a scientific basis for relevant policy formulation.

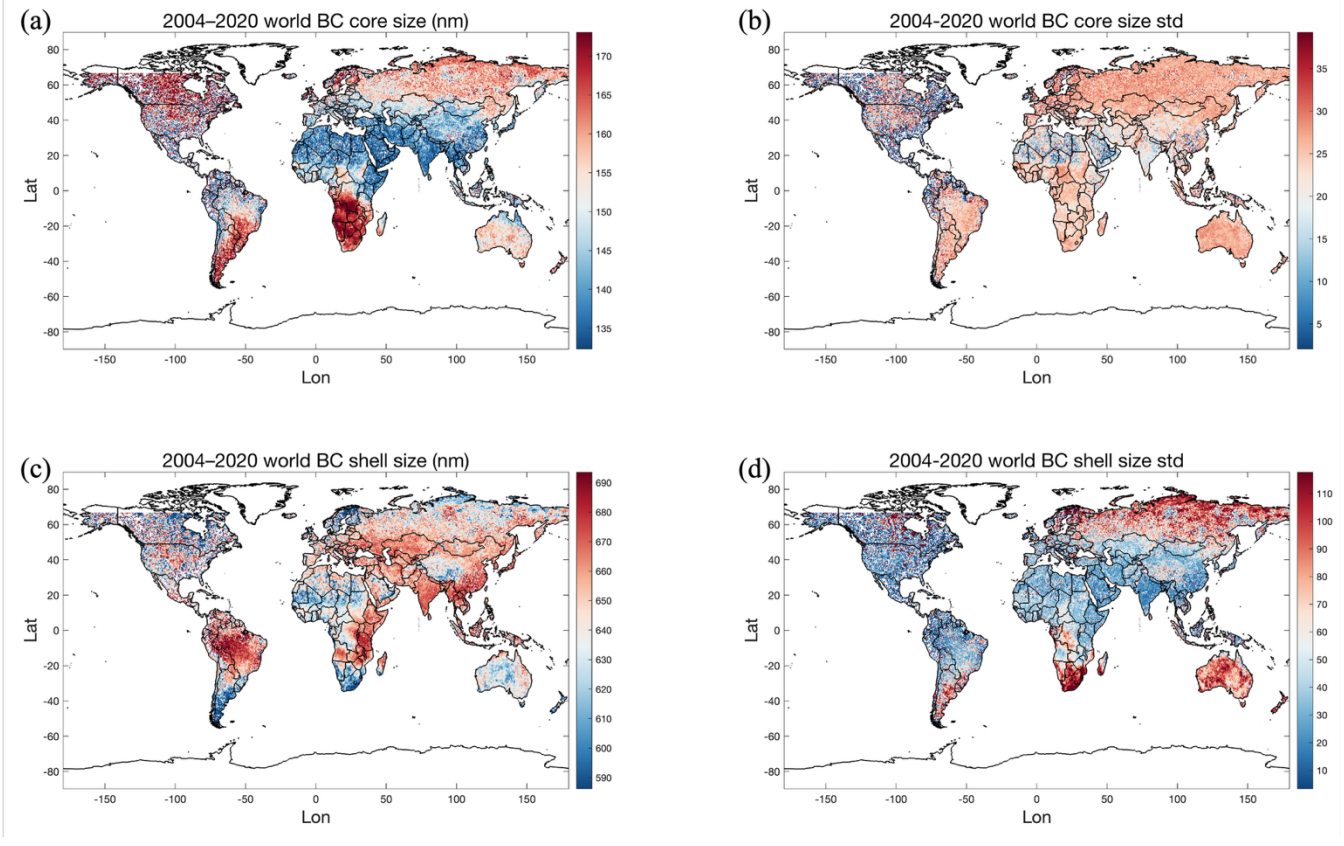

https://doi.org/10.5194/essd-2025-593
Preprint. Discussion started: 7 October 2025

Figure 2. Schematic diagram of global terrestrial products with BC core and shell particle sizes from 2004 to 2020. (a) Mean size of BC core. (b) BC core size standard deviation. (c) Mean size of BC shell. (d) Standard deviation of BC shell size.

Figures 2a and 2b depict the global distribution of BC core diameters and their standard deviations during 2004–2020. Larger BC particle sizes (indicated in red, ranging from 160 to 170 nm) are observed in central and southern Africa, parts of South America, forested and densely populated regions of North America, core urban areas of Europe, and much of Asia. In central and southern Africa, the standard deviation of BC sizes remains relatively balanced (orange, between 20 and 25 nm). The relatively large particle size in these regions is likely linked to widespread biomass burning (e.g., agricultural residue burning and forest fires), where BC generation tends to be stable, less affected by human disturbances, and associated with relatively uniform pollution sources. By contrast, in Europe and large parts of Asia, the standard deviation of BC size is considerably higher (orange to red, 30–35 nm). In Europe, this is primarily attributed to industrial activities and traffic emissions related to high population density, whereas in Asia, in addition to industrial and demographic factors, biomass burning from agriculture, domestic activities, and wildfires also plays an important role. The pronounced variability in particle size in these regions reflects the destabilizing effects of anthropogenic production processes and the uncertainty of wildfire occurrence on BC formation. In North America, BC size variation is more irregular, highlighting the complexity of biomass burning emissions caused by sporadic forest fires, while urban areas exhibit patterns comparable to those in Europe. In South America, regions with larger BC particle sizes also display greater variability: urban centers correspond to anthropogenic sources, whereas in and around the Amazon rainforest, larger BC particles are sporadically observed, likely resulting from frequent deforestation and burning, with biomass burning showing a non-cyclical nature.

The shell size of particles reflects the extent to which BC cores accumulate secondary substances in the atmosphere. As shown in Figures 2c and 2d, relatively large shell sizes (red, exceeding 670 nm) are concentrated in southeastern Africa, northern South America, and across South, Southeast, and East Asia. The increase in shell size in these regions is likely associated with the mixing of BC with other aerosol species, particularly during biomass burning and agricultural waste processing. For instance, in northern Amazonia, shell sizes are substantial but exhibit little variability, suggesting persistent biomass burning as a long-term source with relatively low emission fluctuations. Similar patterns are also found in the central African grassland regions. In parts of Asia, such as China, India, and Southeast Asia, shell sizes generally exceed 650 nm. In Southeast Asia, although the distribution is patchy, the variability remains relatively modest. This can be attributed to frequent, stable biomass burning and intensive emissions from mining and industrial activities, which facilitate the adsorption of additional pollutants, leading to larger shells. The scattered higher variability in Southeast Asia may be linked to seasonal shifts in emissions, particularly differences in biomass burning activities between wet and dry seasons. By contrast, in northern Europe and urban areas of North America, shell sizes are relatively smaller (blue, below ~610 nm) and exhibit low standard deviations (blue to green), indicating greater stability. This pattern likely reflects the effects of stricter environmental regulations and emission controls, which suppress shell growth, reduce the particles' capacity to adsorb additional material, and minimize fluctuations in pollutant emissions.

https://doi.org/10.5194/essd-2025-593
Preprint. Discussion started: 7 October 2025

3.3 Global Analysis of Black Carbon Column Mass and Number Concentrations

In Section 3.2 of the Mie scattering model calculations, as the set of particle radii (R) is determined, the study simultaneously obtains absorption efficiency (Q_{abs}) across various particle size combinations. Using these calculated absorption efficiencies and applying Eq. (9), we further derive the overall absorption coefficient (σ_{abs}) for individual particles. The absorption coefficient is a key parameter describing the particle's ability to absorb light at specific wavelengths and serves as a fundamental basis for studying aerosol optical properties. The accurate calculation of σ_{abs} provides essential insight into aerosol absorption characteristics, particularly in understanding absorption differences among various components.

With σ_{abs} determined, we can utilize the AAOD observational data provided by the MISR satellite and apply Eq.(10) to estimate the particle column number concentration (N_{col}) in the atmosphere. Column number concentration reflects the particle count within an atmospheric column and is a critical metric for describing aerosol distribution and total quantity, particularly crucial for assessing its spatiotemporal variation characteristics.

Further, through Eqs.(11) and (12), we can calculate the particle column mass concentration (M_{col}) based on the column number concentration, where ρ denotes particle density, and M represents the mass of a single BC particle. This result provides a robust computational basis for evaluating the mass of BC particles in the atmosphere, especially valuable for quantifying the contribution of BC to atmospheric pollution and climate change.

This comprehensive calculation framework, which integrates particle size, absorption efficiency, absorption coefficient, as well as number and mass concentrations, establishes a systematic and rigorous physical model. It enables a detailed representation of the spatiotemporal distribution of BC and other aerosol particles in the atmosphere and provides reliable data support for quantifying their mass characteristics. This framework establishes an essential theoretical foundation for subsequent research on the effects of aerosols on climate and the environment, particularly for evaluating the potential impact of BC on global radiative balance and climate warming, highlighting significant applied value.

$$\sigma_{abs} = [\pi(2R)^2/4] \cdot Q_{abs} \quad (9)$$

$$N_{col} = AAOD/\sigma_{abs} \quad (10)$$

$$M = \rho \cdot \frac{4}{3}\pi R^3 \cdot N_{col} \quad (11)$$

$$M_{col} = N_{col} \cdot M \quad (12)$$

https://doi.org/10.5194/essd-2025-593
Preprint. Discussion started: 7 October 2025

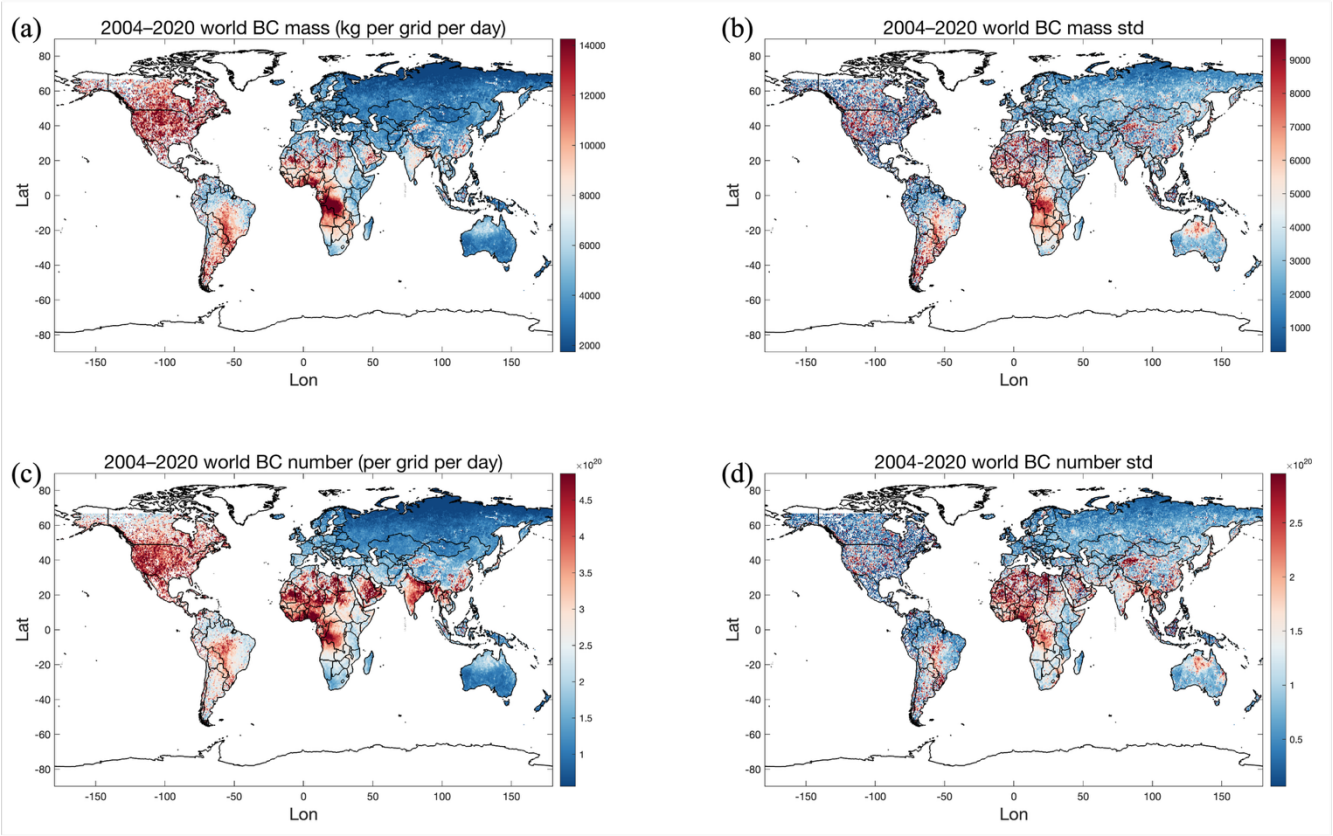

Figure 3. Schematic diagram of global terrestrial products with BC column mass and number concentration from 2004 to 2020. (a) Mean mass concentration of BC column. (b) Standard deviation of BC column mass concentration. (c) Mean number concentration of BC columns. (d) Standard deviation of BC column number concentration.

Figures 3a and 3b illustrate the global distribution of BC column mass concentration and its standard deviation from 2004 to 2020. Pronounced BC mass concentrations, exceeding 8000 kg per grid per day, are observed over central and southern Africa, parts of North America, and central to southern South America. These elevated concentrations are primarily attributed to biomass burning. In contrast, regions such as the Amazon rainforest exhibit moderate BC concentrations, typically ranging between 6000 and 8000 kg per grid per day, which may be linked to agricultural activities and deforestation. Several densely populated areas of Asia, including China, Japan, and Southeast Asia, also show relatively high BC mass concentrations, reflecting the combined influence of industrial activity, transportation emissions, and agricultural practices. Conversely, most regions in Europe and Australia report comparatively low BC concentrations, generally below 6000 kg per grid per day, a pattern likely shaped by stringent air pollution controls that effectively limit BC emissions. Central and western Africa also stand out with both high emission intensity and substantial standard deviations (around 8000 kg per grid per day), indicating strong interannual variability associated with seasonal differences in biomass burning. Elevated variability is likewise observed in parts of East and Southeast Asia, as well as northern Australia, suggesting the combined influence of multiple pollution sources and fluctuating emission dynamics. By comparison, much of South

https://doi.org/10.5194/essd-2025-593
Preprint. Discussion started: 7 October 2025

America exhibits moderate standard deviations, pointing to relatively greater temporal variability, while regions such as southern Australia and much of Europe display lower variability, consistent with more stable emission conditions.

Figures 3c and 3d present the global distribution of BC column number concentration and its standard deviation during the same period. Overall, the spatial distribution of number concentration broadly mirrors that of mass concentration, with notable differences in northwestern Africa, the Arabian Peninsula, and South Asia, where number concentrations appear relatively higher. This discrepancy likely reflects spatial heterogeneity in emission sources as well as differences in BC particle size distributions. In the northwestern African region, high population density and industrial activity are major contributors to the emission of smaller BC particles. In South America, areas characterized by high mass concentrations also exhibit similarly extensive coverage in number concentration, underscoring the role of biomass burning and agricultural activities in generating and dispersing large quantities of BC particles. Regarding variability, central and northwestern Africa exhibit pronounced fluctuations, indicating marked temporal inconsistency in emissions. In South America, variability in number concentration is largely confined to limited areas such as Brazil, São Paulo, and scattered southern regions, while the overall continent demonstrates relatively stable BC emissions.

https://doi.org/10.5194/essd-2025-593
Preprint. Discussion started: 7 October 2025

Table 1. Annual average of BC atmospheric column mass concentration in 9 regions from 2005 to 2020. Region codes are defined as follows: NA1 = North America, SA2 = South America, E3 = Europe, A4 = Africa, EA5 = East Asia, SEA6 = Southeast Asia, SA7 = South Asia, NA8 = North Asia, O9 = Oceania.

BC MASS	NA1	SA2	E3	A4	EA5	SEA6	SA7	NA8	O9
2005	11224	8350	4449	8275	4570	6040	5408	2548	3064
2006	12391	8465	4664	8241	4999	6488	5862	3096	3478
2007	12024	10418	4556	7288	4753	6464	5603	2622	4426
2008	12155	7712	4112	7860	5381	6380	6269	2941	3125
2009	11126	7319	4573	7943	4854	7159	6940	2536	3515
2010	12250	9642	4439	8191	5122	5865	5989	2907	3172
2011	11367	8246	4203	8058	4338	6303	5906	2590	5858
2012	10864	9521	4295	8155	4741	6165	6210	2843	4951
2013	10944	7947	4494	8227	4899	5949	6037	2746	3107
2014	11896	7854	4312	7391	4668	5991	5686	2700	3625
2015	10962	7473	4557	7964	4641	5816	5978	2794	3209
2016	12252	8552	4988	8087	4675	5057	6122	2659	3047
2017	11397	8062	5090	8245	4408	5266	6005	2957	4254
2018	10194	7495	4398	7911	4657	5485	7198	2650	3369
2019	11053	9037	3952	7558	4157	5706	6020	2533	3277
2020	13167	9259	4966	7793	4224	5300	6446	2630	2977

As shown in Table 1, the annual mean BC column mass concentrations are reported for nine regions, while the corresponding column number concentrations, core sizes, and shell sizes are provided in Tables C1, C2, C3. For North America, BC column mass concentrations increased during 2005–2007, declined slightly between 2008 and 2012, and thereafter exhibited a fluctuating upward trend, reaching a maximum in 2020. Column number concentrations remained relatively high with minor fluctuations, followed by a pronounced increase in 2020. Core size showed little variation (157–161 nm) and did not peak in 2020, while shell size fluctuated during 2005–2015 and showed minor variability thereafter without a monotonic trend. By contrast, South America experienced a rise in BC mass concentrations during 2005–2007, a decline in 2008–2009, and another increase in 2010, followed by sustained high but fluctuating levels. Number concentrations were elevated in 2005–2007, decreased between 2008 and 2012, and exhibited alternating downward and upward tendencies after 2013. Core size increased gradually from ~151 nm in 2005 to above 159 nm by 2012, thereafter remaining high. Shell size stayed elevated during 2005–2015, with slight increases, and fluctuated after 2016 without a long-term decline. In Europe, BC mass concentrations remained relatively stable, fluctuating slightly between 4000 and 5000 kg per grid per day from 2005 to 2020. Number concentrations also stayed within a stable range with only minor variability. Core size peaked in 2016 (above 155 nm), while shell size fluctuated between ~630 and 640 nm without a monotonic trend.

https://doi.org/10.5194/essd-2025-593
Preprint. Discussion started: 7 October 2025

A similar pattern is observed in Africa, where both BC mass and number concentrations decreased slightly during 2005–2007, rose again in 2008, and subsequently remained at relatively high levels with modest variability after 2014. Core size stayed within 148–152 nm, showing only minor declines, while shell size remained around 639–645 nm without a discernible long-term trend. In East Asia, BC mass concentrations rose from 2005 to 2008 and then declined overall, reaching their lowest level in 2019. Number concentrations were relatively stable during 2005–2012 but decreased thereafter. Core size fluctuated between 144 and 149 nm, with a slight downward tendency. Shell size remained consistently between 647 and 653 nm throughout the period. For Southeast Asia, BC mass concentrations increased during 2005–2009, then declined and stabilized at lower levels. Number concentrations followed a similar trajectory, peaking during 2005–2009 before declining after 2010. Core size remained within 143–146 nm, showing little variation. Shell size was relatively high (655–660 nm) in 2005–2010, followed by a gradual decline and subsequent stabilization. In South Asia, BC mass concentrations increased during 2005–2009, fluctuated between 6000 and 7000 kg per grid per day thereafter, and showed a distinct peak in 2018. Number concentrations followed a similar pattern, remaining high after 2010 and peaking in 2018. Core size declined overall, while shell size fluctuated between 657 and 663 nm without a monotonic trend. For North Asia, BC mass and number concentrations remained low and stable, with no significant long-term trends. Core size peaked in 2008 and then declined, stabilizing between 151 and 155 nm. Shell size showed limited variability, with a slight decreasing tendency and a minimum in 2008. Finally, Oceania exhibited increasing BC mass concentrations during 2005–2007, a decline from 2008 to 2012, and subsequent fluctuations within 3000–4000 kg per grid per day, with notable peaks in 2011 and 2012. Number concentrations showed a similar temporal pattern. Core size was more variable, and shell size displayed even greater fluctuations, with marked decreases in 2011 and 2017.

3.4 Sensitivity analysis under different mixed states

A sensitivity analysis of MISR-derived BC data for 2005–2020 was conducted based on different core-shell size combinations, using percentiles (25%, 50%, 75%) and the mean. Differences were evaluated across BC column mass concentration (MASS), column number concentration (NUM), core particle size (BCsize), and coating size (Shellsize). Time series and probability density functions (PDFs) highlight the sensitivity of MISR retrievals across different concentration and size ranges.

Figure 4a presents time series of BC properties derived from different percentiles. For both column mass and number concentrations, the 50th percentile and the mean show nearly identical temporal patterns, particularly during high-concentration seasons (e.g., spring and summer), where peaks and fluctuations align closely. This consistency indicates that both metrics effectively capture background concentration trends and are well suited for monitoring long-term variability, with limited sensitivity to particle size assumptions. By contrast, the 75th percentile exhibits stronger variability and higher peaks during pollution episodes, reflecting enhanced sensitivity to high-concentration events. This makes the 75th percentile more appropriate for identifying extreme pollution episodes and rapid concentration increases. The 25th percentile remains

https://doi.org/10.5194/essd-2025-593
Preprint. Discussion started: 7 October 2025

345 comparatively stable with lower values and smaller fluctuations, providing reliable information on background low-concentration conditions.

For BC core and shell sizes, differences among percentiles are more pronounced. The 75th percentile consistently yields larger sizes than the 50th and 25th percentiles, particularly during periods of high concentration or large-particle events, with peaks notably higher than the mean. This demonstrates MISR's enhanced sensitivity to large BC particles when higher 350 percentiles are applied, making the 75th percentile suitable for monitoring extreme conditions and large-size regimes. In contrast, the 50th percentile and the mean display smoother temporal variations and similar overall trends, representative of typical mid-size particle distributions. The mean is slightly lower than the 50th percentile, suggesting that it integrates a broader range of particle sizes, including larger ones, and is thus suitable for characterizing overall distributions. The 25th percentile remains lowest, with minimal variability, emphasizing its relevance for representing small-particle conditions in 355 relatively clean environments.

The PDFs (Figure 4b) further illustrate these percentile-dependent sensitivities. For column mass and number concentrations, the 50th percentile and the mean show largely overlapping distributions, with similar frequency patterns, underscoring their robustness in representing general conditions. The 75th percentile shifts toward higher concentration ranges, with elevated frequencies, highlighting MISR's responsiveness to extreme pollution. The 25th percentile is concentrated in the low-360 concentration range, confirming its suitability for background monitoring. For BC core and shell sizes, the distributions diverge more strongly. The 25th percentile peaks at smaller size ranges, characterizing small-particle populations. The 50th percentile has a slightly broader distribution than the mean, covering more of the large-size range and reinforcing its representativeness under both background and polluted conditions. The 75th percentile is skewed toward much larger sizes, with substantially higher frequencies, indicating strong sensitivity to large-particle BC and supporting its use in high-365 pollution, large-size analyses. The mean overlaps largely with the 50th percentile, capturing overall particle size information across most conditions.

Overall, the use of multiple percentiles provides a layered characterization of MISR sensitivity. The 50th percentile and mean are most effective for describing general BC concentrations and typical size distributions, while the 75th percentile highlights high-concentration and large-particle events, and the 25th percentile emphasizes low-concentration and small-370 particle conditions. Together, these metrics offer complementary perspectives for refined monitoring of BC under diverse atmospheric environments.

https://doi.org/10.5194/essd-2025-593
Preprint. Discussion started: 7 October 2025

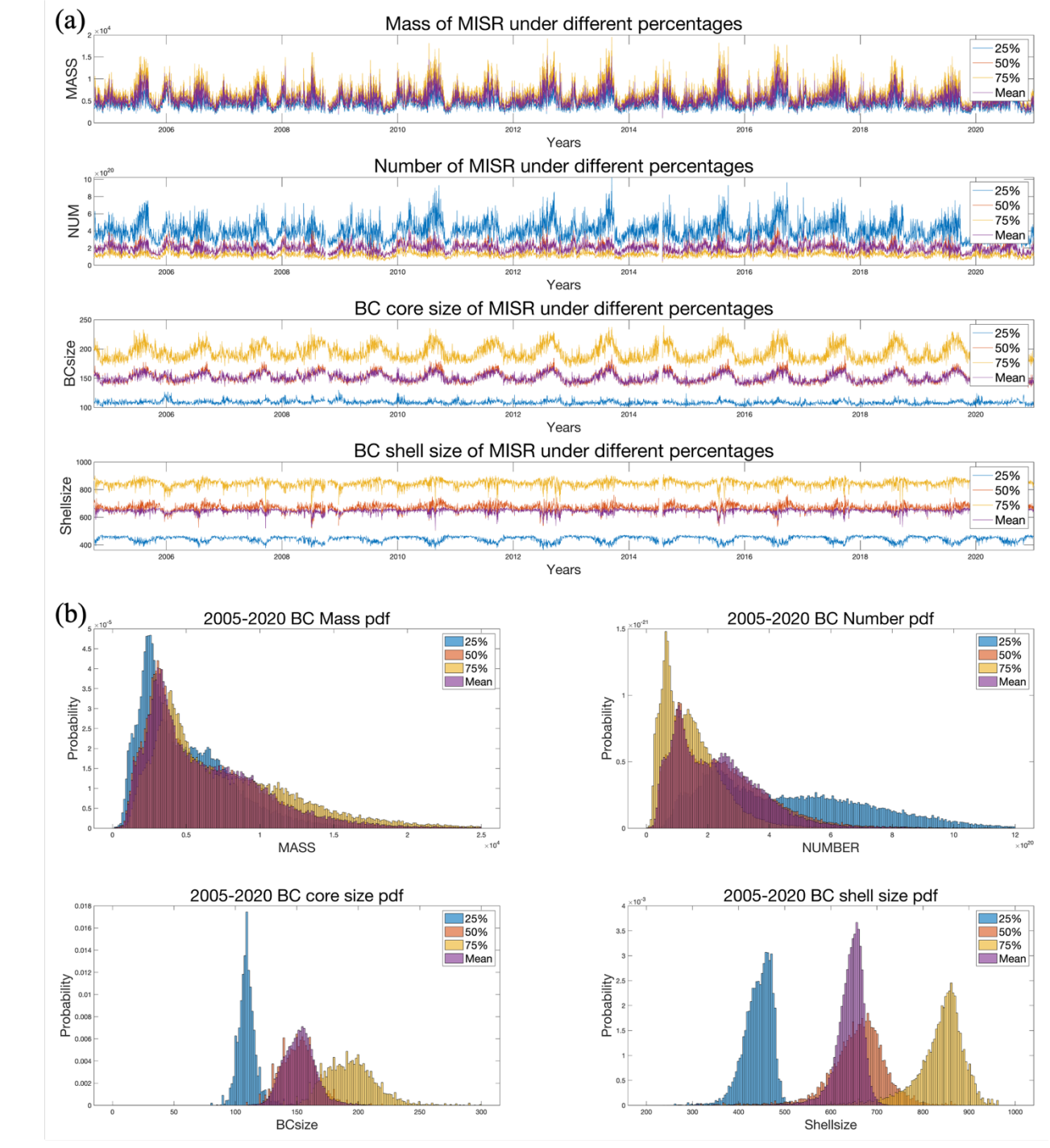

Figure 4. Sensitivity analysis of various characteristics of BC under different percentages of core-shell sizes. (a)Time series analysis, from top to bottom, including BC column mass concentration, column number concentration, core size, and shell size. (b) PDF analysis of BC mass concentration, column number concentration, core size, and shell size.

https://doi.org/10.5194/essd-2025-593
Preprint. Discussion started: 7 October 2025

3.5 Comparative Analysis of Black Carbon Observations: Insights from MERRA and MISR Datasets Across Global Regions

To better compare BC column mass concentrations derived from different data sources, this study implemented a rigorous matching and screening procedure between MISR and MERRA. Specifically, daily grid-level MISR retrievals were first filtered and used as the reference, and the corresponding MERRA reanalysis data were extracted within the same spatiotemporal domain to ensure consistency in both spatial resolution and temporal scale. Based on this framework, comparative analyses were conducted under different concentration regimes (e.g., low versus high levels) and particle size assumptions (small versus large sizes). Such a daily grid-level matching strategy effectively minimizes systematic biases arising from differences in spatial and temporal resolution, thereby ensuring that the comparisons between MISR and MERRA are both representative and physically meaningful. Moreover, this approach provides a robust basis for assessing the applicability and limitations of the two datasets across different regions, emission conditions, and climatic contexts.

Figures 5a and 5b illustrate that MISR and MERRA exhibit substantial discrepancies in the global distribution of BC column mass concentrations. MISR generally reports higher BC levels in Africa, South Asia, and East Asia, particularly over central-southern Africa, the Indian subcontinent, and both coastal and inland Chinese urban areas, whereas MERRA estimates are consistently lower. Only in limited regions, such as parts of Southeast Asia, does MERRA show relatively elevated signals, though it still tends to underestimate regional emissions overall. In South America, MISR detects enhanced concentrations over the Amazon basin and southern regions, while MERRA shows weaker signals, indicating lower sensitivity to localized emission sources. In Europe and North America, both datasets reveal generally lower BC concentrations; however, MISR captures more localized pollution signals associated with industrial activity and wildfires, whereas MERRA remains comparatively smoother. In Oceania, MISR reports relatively higher concentrations in the north, while MERRA indicates higher values in the west.

Figure 5c presents the MISR-to-MERRA ratio, highlighting spatial differences between the datasets. Ratios exceeding unity dominate across much of Africa, South Asia, East Asia, and most of China, reflecting substantially higher BC estimates from MISR and its stronger sensitivity to local emission sources. Conversely, ratios near or below unity occur in northern South America, southern and central Australia, and parts of central and western Africa, suggesting higher MERRA estimates in those regions. Overall, MISR yields substantially higher ratios in major emission hotspots, enabling clearer identification of localized pollution sources, whereas MERRA tends to emphasize background concentrations. In Europe, both datasets report relatively low BC, but their absolute values differ considerably: MISR captures greater spatial heterogeneity linked to industrial emissions and reports higher estimates overall. In North America, due to MISR's AOD > 0.25 threshold constraint, significant BC is retrieved primarily over fire-affected regions and eastern urban centers, with MISR values far exceeding MERRA, indicating that MERRA strongly underestimates episodic events. Over Oceania, where overall BC concentrations are low, the two datasets show broadly consistent patterns across much of the central region; however, MERRA reports higher concentrations in the west (e.g., around Perth).

https://doi.org/10.5194/essd-2025-593
Preprint. Discussion started: 7 October 2025

Figure 5d compares the probability density functions (PDFs) of BC mass concentrations from the two datasets. MERRA exhibits a distribution concentrated in the low-concentration range, indicating its stronger capability in characterizing large-scale background conditions. By contrast, MISR shows higher frequencies in the elevated concentration range, highlighting its advantage in capturing localized high-pollution events, especially over South America, South Asia, and East Asia–consistent with the spatial ratio patterns shown in Fig. 5c.

Figure 5e shows the MISR-to-MERRA ratio distribution under relatively low concentration conditions (MISR Mean25%). Compared with the mean ratio map, the overall ratios are closer to 1, indicating higher consistency between MISR and MERRA at lower MISR concentrations. However, in regions such as central–western Africa, southern Australia, and parts of South America, areas with ratios below 1 become more pronounced, suggesting that MISR estimates are lower than those of MERRA. Over most of China, the ratio differences remain relatively small (within a factor of 1–2), reflecting a certain degree of consistency. In northern Asia, the ratio declines, which may be related to MISR's detection sensitivity, the characteristics of local emission sources, and algorithmic uncertainties. Nevertheless, in northern Europe and South Asia, the MISR-to-MERRA ratios remain elevated, highlighting MISR's stronger sensitivity to localized pollution sources.

Figure 5f presents the ratio distribution under relatively high concentration conditions (MISR Mean75%). Most regions exhibit ratios significantly greater than 1, especially southern Africa, the Indian subcontinent, and East Asia, where MISR estimates far exceed those of MERRA. This indicates that MISR responds more strongly to BC in high-concentration regions, enabling clearer identification of emission sources and their intensities. In southwestern Australia and certain parts of western and central Africa, the ratios fall below 1, though the differences are limited in both spatial extent and magnitude. In eastern China, India, and some high-emission areas of Southeast Asia, MISR values are particularly pronounced, reflecting the distinctive imprint of high-pollution events in its observations.

Figure 5g shows the ratio distribution based on the small-size assumption (MISR Size25%). Its spatial pattern closely resembles that in Fig. 5c, underscoring the stronger sensitivity of small-size BC concentrations to localized emissions. Because smaller BC particles have longer atmospheric lifetimes and can be transported over broader regions, they produce stronger pollution signals in urban and industrial areas. Moreover, small-size BC is more responsive to meteorological conditions (e.g., temperature, humidity), resulting in more pronounced regional heterogeneity, particularly over parts of South America, Africa, and Asia.

Figure 5h presents the ratio distribution under the large-size assumption (MISR Size75%). Similar to Fig. 5c, its spatial distribution appears smoother, with relatively uniform ratios. This reflects the properties of large-size BC, which settles more rapidly and has a shorter atmospheric lifetime, thus remaining concentrated near emission sources and producing more homogeneous large-scale distributions. Notably, the overall ratios in Fig. 5h are slightly lower than those in Fig. 5c, indicating that while MISR remains more responsive to local emissions than MERRA under the large-size assumption, the overall differences are smaller.

Taken together, Figs. 5e and 5f illustrate the differences between MISR and MERRA across concentration levels: MISR is more sensitive in high-concentration regions, while agreement with MERRA is higher under low concentrations. Figs. 5g

https://doi.org/10.5194/essd-2025-593
Preprint. Discussion started: 7 October 2025

and 5h reveal contrasting behaviors under particle size assumptions: small-size BC better captures localized sources and transport features, whereas large-size BC is more spatially concentrated with smaller overall differences. These variations reflect the complexity of BC transport, deposition, and source impacts in the atmosphere. Overall, MISR demonstrates stronger sensitivity to high concentrations and localized sources, whereas MERRA more consistently reflects large-scale background distributions.

In terms of global BC column concentration patterns, the two datasets show distinct characteristics. MERRA, being a model-based reanalysis product, exhibits relatively continuous and smooth spatial gradients. Across global regions, MERRA generally captures broad-scale concentration trends, particularly over high-BC regions in Africa, South America, Australia, and Asia, but with limited representation of localized details. In contrast, MISR, based on multi-angle imaging, provides higher spatial resolution and stronger sensitivity to local variability, yielding richer spatial heterogeneity. The MISR-to-MERRA ratio maps highlight that MISR estimates are substantially higher over regions such as sub-Saharan Africa and eastern South America, underscoring its responsiveness to strong emission sources. MISR also reveals more pronounced spatial variability within regions, particularly in high-emission areas such as South Asia, East Asia, and southern South America. This variability likely reflects the advantages of MISR's multi-angle observational approach, which captures localized fluctuations and gradients in BC concentrations that MERRA tends to smooth over.

https://doi.org/10.5194/essd-2025-593
Preprint. Discussion started: 7 October 2025

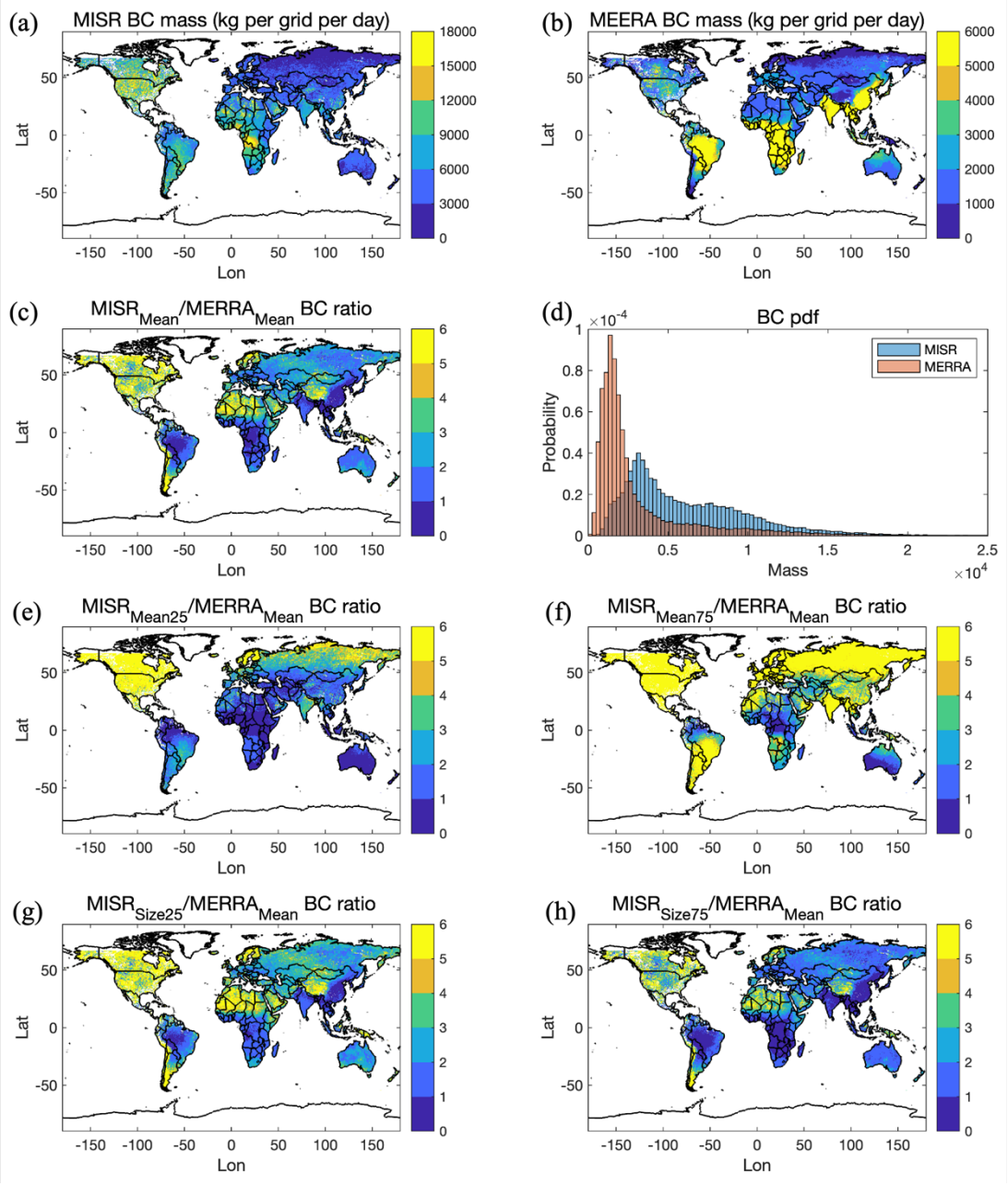

Figure 5. Comparison between BC column concentration estimated based on MISR and MERRA data. (a)MISR BC column mass concentration. (b)MERRA BC column mass concentration. (c)Ratio of mean BC column mass concentration between MISR and MERRA. (d)PDF of mean BC column mass concentration between MISR and MERRA. (e)Ratio of BC column mass concentration between MISR (25% of mean) and MERRA (mean) (f)Ratio of BC column mass concentration between MISR (75% of mean) and MERRA (mean). (g) Ratio of BC column mass concentration between MISR (25% of size) and MERRA (mean). (h) Ratio of BC column mass concentration between MISR (75% of size) and MERRA (mean).

https://doi.org/10.5194/essd-2025-593
Preprint. Discussion started: 7 October 2025

4 Discussion

Following the retrieval of column number and mass concentration products of BC, rigorous mass control and multi-dimensional filtering were applied to ensure the scientific robustness and reliability of subsequent analyses. Specifically, three main constraints were introduced: the number of valid observational days, the column number concentration of BC, and the $AAOD_{443/865}$ ratio. First, regional-scale statistics without sufficient temporal coverage can be strongly biased by occasional events, thereby reducing representativeness (Chen and Prinn, 2006). By imposing a minimum threshold on valid days, the temporal stability and comparability of the dataset are maintained. Second, BC column number concentration is a direct indicator of BC loading in the atmosphere, yet its distribution may include outliers due to extreme or abnormal events, points with lower-confidence results. If left unfiltered, these values could distort averages and obscure the underlying atmospheric signal. Thus, appropriate thresholding was applied to exclude clearly unrealistically high or low-pollution cases. Finally, the $AAOD_{443/865}$ ratio was incorporated as an optical constraint (Bergstrom et al., 2007; Russell et al., 2010; Helin et al., 2021; Bigi et al., 2023). This ratio characterizes aerosol absorption across spectral bands and, when abnormally high, may indicate the presence of strongly absorbing non-BC aerosols which are large in size, specifically dust. By applying this filter, potential dust contamination was effectively reduced, thereby improving the specificity and robustness of the retained data. Through these combined constraints, data reliability was enhanced in terms of temporal coverage, concentration levels, and optical properties, ensuring that the subsequent analysis reflects the contribution of BC with greater accuracy.

It is important to note, however, that regional differences in climatic background, emission source structures, and aerosol types necessitate adaptive filtering strategies. A uniform threshold across all regions may lead to excessive sample loss in some areas or insufficient removal of anomalous cases in others, potentially biasing the results. To address this, a region-specific approach was adopted, selecting appropriate percentile-based thresholds or quantile criteria according to local data distributions. This method not only maximizes data representativeness but also removes samples with limited explanatory power. By incorporating such regionally adaptive criteria, the dataset better reflects the true atmospheric processes and BC pollution characteristics across different environments. After these mass control and filtering steps, the final sample set is both stable and credible, providing a solid basis for in-depth investigations into BC concentration levels, spatiotemporal.

4.1 Characteristics Over an Example Biomass Burning Region

The results in Figure 6 show that the filtered regions are mainly concentrated in central and southern South America, where multiple mass-control criteria valid observational days, BC number concentration, and optical ratio are simultaneously satisfied, yielding high-mass samples with clear biomass-burning signatures based on both the underlying land types (forests, savannas, etc.) and high annual temporal variation with both inter- and intra-annual variation (Cohen et al., 2011; Cohen and Wang, 2014). Although some regions may exhibit extremely high values, they were excluded from the analysis due to insufficient observational coverage. The focus of this study is on representative and robust distributional patterns, thereby ensuring statistical stability and reducing uncertainties caused by isolated outliers.

https://doi.org/10.5194/essd-2025-593
Preprint. Discussion started: 7 October 2025

From the filtered spatial distribution, high-value areas are primarily located in the Pantanal wetlands and the surrounding parts of the Amazon Basin, where fire activity is intense during the dry season and biomass burning has long been recognized as the dominant source of emissions (Krol et al., 2013). The spatial overlap between the filtered results and these well-known fire clusters demonstrates that the applied BC concentration constraints effectively capture biomass-burning–dominated aerosol signals (Freire et al., 2020). This spatial consistency underscores the physical robustness of the processed dataset, allowing the retrieved BC distribution to reflect biomass burning features rather than being masked by dust or other aerosol types.

In these regions, the influence of biomass burning is not confined to the fire source areas but extends across larger spatial scales through atmospheric processing of primary BC and co-emitted secondary aerosol precursors, followed by atmospheric transport and in-situ aging. For example, fires in the Pantanal region generate smoke plumes that can travel hundreds to thousands of kilometers, reaching densely populated urban clusters in the southeast. Such long-range transport events sharply deteriorate air mass and impose severe health risks (Santos et al., 2024). This highlights that the high-value regions identified by the filtering process represent not only centers of fire activity but also critical nodes of pollution transport and regional connectivity, providing key insights into BC transport and deposition processes in the atmosphere.

From a climatic perspective, BC aerosols emitted from biomass burning in South America can perturb the climate system by altering atmospheric radiative balance and cloud formation. Through semi-direct effects, these aerosols can reduce cloud cover and modify atmospheric stability, thereby influencing precipitation patterns and regional energy balance. The strong spatial consistency between the identified high-value regions and the most intense fire areas indicates that BC-related climate effects are tightly coupled with fire activity. This is validated by the long-term AERONET observations from the CUIABA-MIRANDA station located within the identified region, demonstrating a clear correspondence between MISR and AERONET monthly peaks across the years with overlapping records (see Figure B1).

The identified BC hotspots in South America not only reproduce the canonical spatial distribution of biomass-burning belts but also highlight the pivotal role of fire activity in pollution transport and climate feedbacks (Thornhill et al., 2018). These findings provide robust observational evidence for understanding the environmental impacts of biomass burning emissions and emphasize the importance of integrating satellite observations with model simulations in future studies to better elucidate the role of BC in regional atmospheric and climate processes.

https://doi.org/10.5194/essd-2025-593
Preprint. Discussion started: 7 October 2025

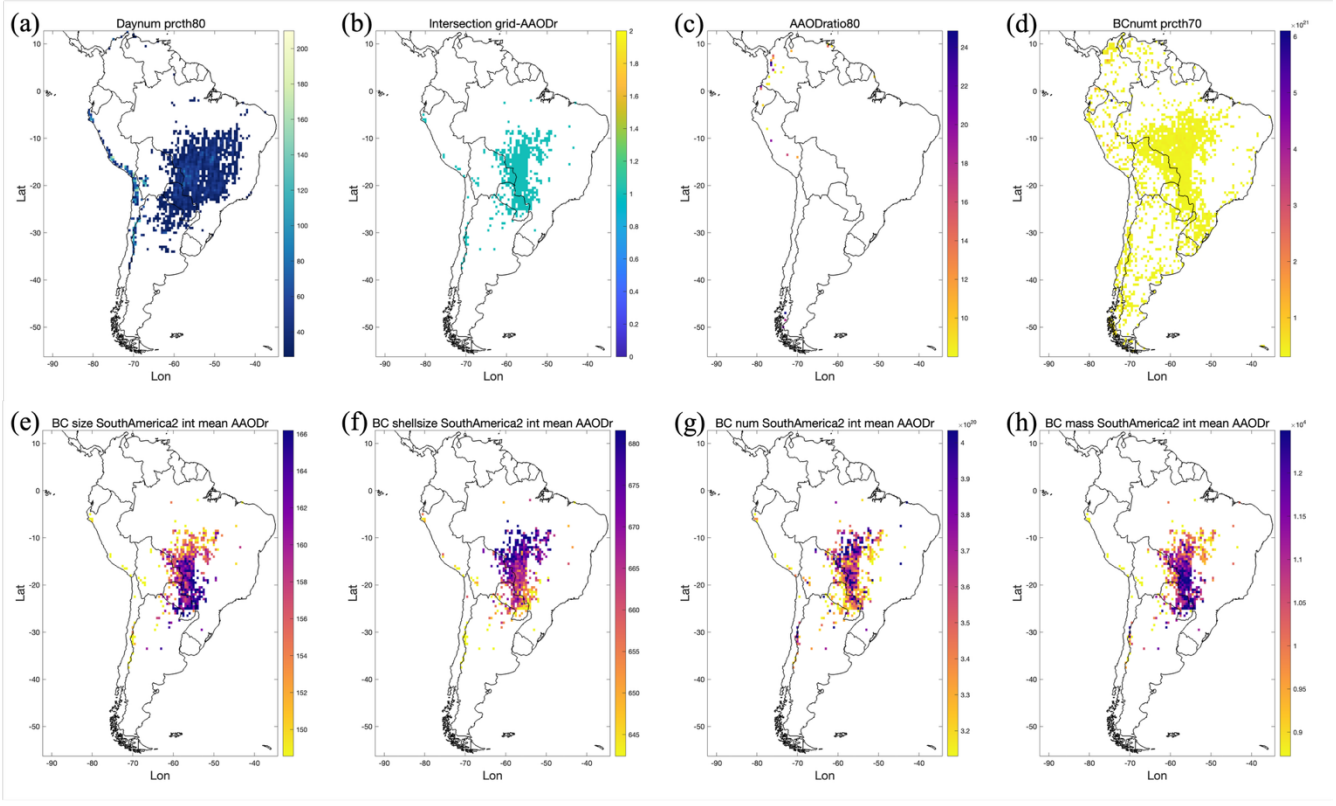

Figure 6. Results of the analysis based on the BC column concentration product over South America. (a) Regions with more than 80% valid observational days. (b) Regions with more than 70% BC column number concentration. (c) Regions excluded due to $AAOD_{443/865}$ values greater than 8.0. (d) Overlapping regions from (a) and (b) after excluding those regions identified in (c). (e) BC column number concentration in the filtered regions. (f) BC column mass concentration in the filtered regions. (g) BC particle size in the filtered regions. (h). BC Shell size in the filtered regions.

4.2 An Example Emission Area Driven by Dense Population and Industrial Activity

Figure 7 shows that the filtered regions are mainly located in southern and central India, where both the number of valid observational days and overall data mass meet the criteria. These regions therefore provide relatively stable and reliable representations of BC distribution. Spatially, although areas such as the Indo-Gangetic Plain and Delhi exhibit high column concentrations, these are observed only over a small number of days. The filtered regions do not cover these traditional hotspots, but are known to be distributed across three areas, namely Maharashtra, Tamil Nadu, and Karnataka, which rank among the leading states in India by GDP, and contain substantial amounts of light and medium industry and high population density (Shaban et al., 2022; Shanmugam and Odasseril, 2024; Ramachandran et al., 2025). This difference suggests that the applied filtering approach favors capturing long-term and persistent emission patterns rather than isolated high-value signals

https://doi.org/10.5194/essd-2025-593
Preprint. Discussion started: 7 October 2025

driven by sparse observations or extreme events. Such processing not only enhances the statistical robustness of the results but also ensures greater representativeness of the identified regions.

In the southern filtered regions, BC number and mass concentrations show strong consistency, with particle size and Shell diameter displaying typical signatures of combustion sources. This distribution is closely linked to local energy-use structures (Huang et al., 2023). In southern India, many households continue to rely heavily on traditional fuels such as firewood, crop residues, and dung cakes. Routine biomass burning in rural areas contributes to a sustained and stable source over these regions. These regions emissions are also strongly coupled with population distribution, leading to spatial BC patterns that align with population density. At the same time, industrial activity and urban emissions are also evident in these regions (Chathurangika et al., 2022). Particularly along industrial corridors and in the vicinity of large- and medium-sized cities, the overlap of combustion and industrial sources further amplifies local pollution levels. While analysis in this region is consistent with known conditions on the ground(Jaganathan et al., 2025; Kawano et al., 2025; Kunjir et al., 2025; Luo et al., 2025), it has generally been overlooked by global-scale emissions databases(Li et al., 2017; Kumar et al., 2023; Ren et al., 2025).

Importantly, this combined influence of biomass burning and industrial emissions is not the result of singular extreme events but rather a persistent and widespread emission regime. Under the modulation of the monsoon system, such emissions are more easily transported and accumulated, thereby exerting prolonged and significant impacts on regional air mass when emissions are continuous(Wei et al., 2022). Unlike South America, where biomass burning is dominated by seasonal wildfires, BC emissions in central and southern India arise from a more complex combination of household energy consumption, agricultural residue burning, and industrial production, leading to environmental impacts that are correspondingly more intricate and persistent.

Overall, the identified regions in India reveal the typical characteristics of biomass burning and energy use in southern and central areas, highlighting the overlapping contributions of rural energy consumption, industrial activity, and urban emissions. These findings suggest that the environmental impacts of BC in South Asia are not confined to the agricultural burning and urban pollution centers in the north but are also deeply embedded in the everyday energy use and industrial emission patterns of the south. These regions play a critical role in driving air mass degradation, altering regional radiative balance, and shaping monsoon-related climate feedbacks. Integrating such observational results with model simulations and health risk assessments will provide a more comprehensive understanding of the long-term implications of these emissions for regional ecosystems and public health.

https://doi.org/10.5194/essd-2025-593
Preprint. Discussion started: 7 October 2025

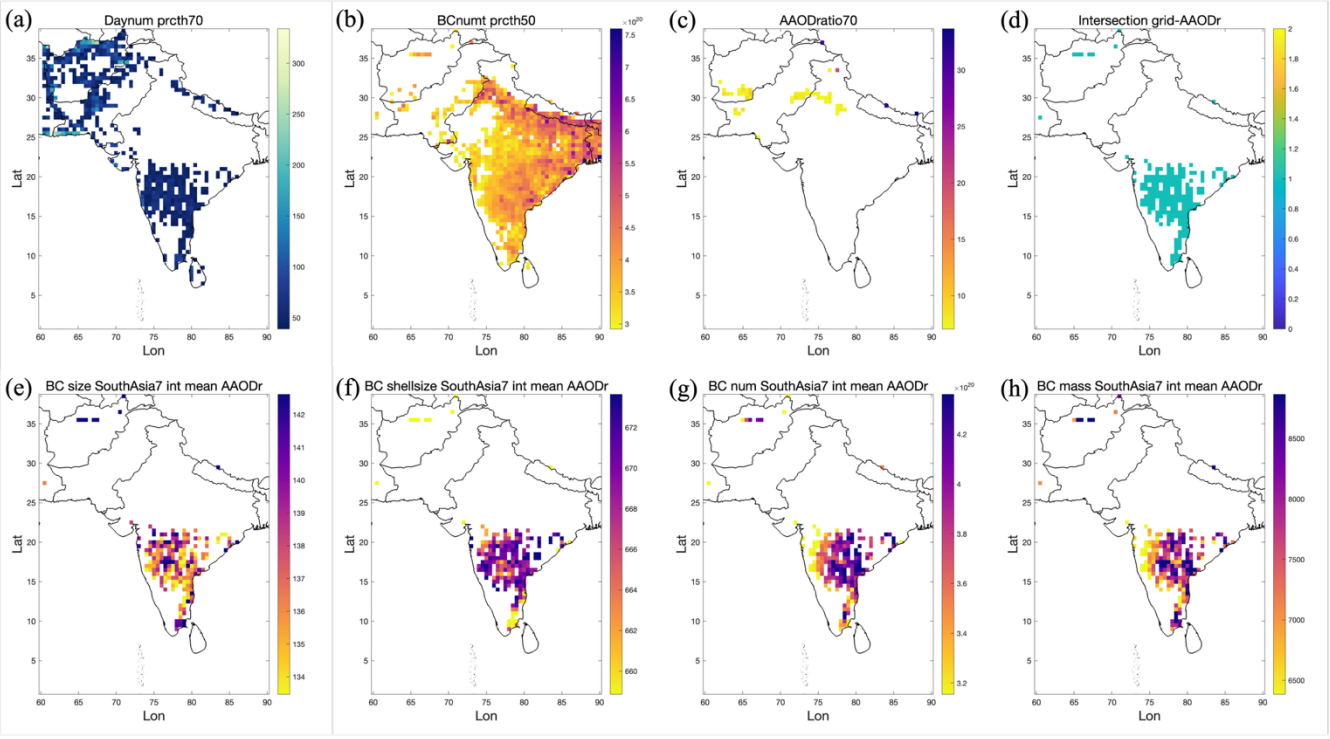

Figure 7. Results of the analysis based on the BC column concentration product over India. (a) Regions with more than 70% valid observational days. (b) Regions with more than 50% BC column number concentration. (c) Regions excluded due to $AAOD_{443/865}$ values greater than 7.0. (d) Overlapping regions from (a) and (b) after excluding those regions identified in (c). (e) BC column number concentration in the filtered regions. (f) BC column mass concentration in the filtered regions. (g) BC particle size in the filtered regions. (h) BC Shell size in the filtered regions.

It is important to emphasize that the filtering strategy applied in this study is designed to capture representative distributional features, with the aim of producing results that are statistically robust and regionally meaningful. However, regions with limited observational samples but potentially extreme values remain areas of concern. For instance, the Indo-Gangetic Plain and the surroundings of Delhi have long been regarded as the most prominent BC emission centers in India. Despite their substantial short-term aerosol emissions and observed high concentration burdens associated environmental and health risks, these areas were excluded from the present analysis due to insufficient valid observational days, with a large number of very clean days also occurring in these regions during other times of the year. While this filtering approach highlights long-term stable patterns, it also underscores that extreme pollution events and observation gaps may result in certain hotspots being underrepresented. Therefore, studies focusing on short-term extremes or localized high-concentration impacts should combine raw observations with targeted monitoring strategies.

In summary, the multi-step filtering method successfully identified the canonical biomass-burning regions in South America, where the spatial distribution, BC concentrations, and particle-size characteristics are consistent with satellite observations and extreme fire events, thereby validating the method and revealing the far-reaching impacts of biomass burning on air

https://doi.org/10.5194/essd-2025-593
Preprint. Discussion started: 7 October 2025

mass, regional climate, and public health. The high-value regions identified in India, by contrast, highlight the combined effects of agricultural burning, industrial activity, and household biomass use, reflecting the long-term contributions of multiple overlapping sources. These regions are not only major drivers of air mass deterioration in South Asia but also key actors in climate feedbacks and health risks. Additional regional details and supplementary results, provided in the supporting materials and full dataset, offer further opportunities for in-depth regional analysis and thematic studies to extend understanding of BC's environmental impacts.

https://doi.org/10.5194/essd-2025-593
Preprint. Discussion started: 7 October 2025

5 Data availability

The original input datasets used in this study, together with the derived BC column concentration products, are publicly available at Figshare with DOI: https://figshare.com/s/2a2aa16468e874d42ab6 (Liu et al., 2025). The MISR aerosol products, AERONET ground-based observations from the CUIABA-MIRANDA site, and the MERRA-2 reanalysis data were used in this study. These external datasets are openly available from their respective providers and are also archived together with the derived products in figshare for consistency and long-term accessibility.

6 Conclusions

This study developed an integrated methodology to estimate global BC column concentrations by combining MISR multi-band satellite retrievals with Mie scattering simulations under single scattering albedo constraints. Through a systematic framework, we retrieved particle size distributions, absorption efficiencies, and subsequently derived BC column number and mass concentrations as well as two microphysical properties at a daily time step and global scale. Comparisons with AERONET and MERRA-2 datasets demonstrated the robustness and reliability of this approach across diverse regions and time periods. The results reveal distinct regional and temporal patterns of BC, highlighting the strong influence of biomass burning, industrial activity, and anthropogenic emissions in shaping both the magnitude and variability of BC concentrations. The methodology significantly enhances the capacity to capture long-term and spatially extensive BC distributions, overcoming key limitations of traditional single-source observations. By providing a physically consistent and observation-driven dataset, this work offers valuable support for climate and air quality modeling, particularly in constraining radiative forcing estimates and assessing the environmental impacts of BC. Future applications of this approach can extend to other absorbing aerosols, improving predictive capability in Earth system models and informing targeted mitigation strategies at both regional and global scales.

7 Author contributions

JBC was responsible for conceptualization and funding acquisition, and also supervised the study. ZL and JBC conducted the formal analysis and validation. ZL and JBC, together with LG and SW, developed the methodology. ZL performed the software development, data processing, and visualization. ZL and JBC carried out the investigation, with additional resources provided by SW and ZL. The original draft was prepared by ZL, JBC, and PT, while JBC, ZL, PT, and KQ contributed to review and editing.

8 Competing interests

The authors declare that they have no conflict of interest.

https://doi.org/10.5194/essd-2025-593
Preprint. Discussion started: 7 October 2025

9 Acknowledgements

We acknowledge the MISR science team for providing the MISR products used in this study. We also acknowledge the AERONET principal investigator and staff at the CUIABA-MIRANDA site for maintaining and providing high-quality ground-based aerosol observations. In addition, we acknowledge the NASA Global Modeling and Assimilation Office (GMAO) for providing the MERRA-2 reanalysis data.

10 Financial support

This work was supported by the National Natural Science Foundation of China (Grant No.42075147) and the Fundamental Research Funds for the Central Universities (Grant No.2023KYJD1003).

https://doi.org/10.5194/essd-2025-593
Preprint. Discussion started: 7 October 2025

Open Access Earth System Science Data Discussions

Appendix

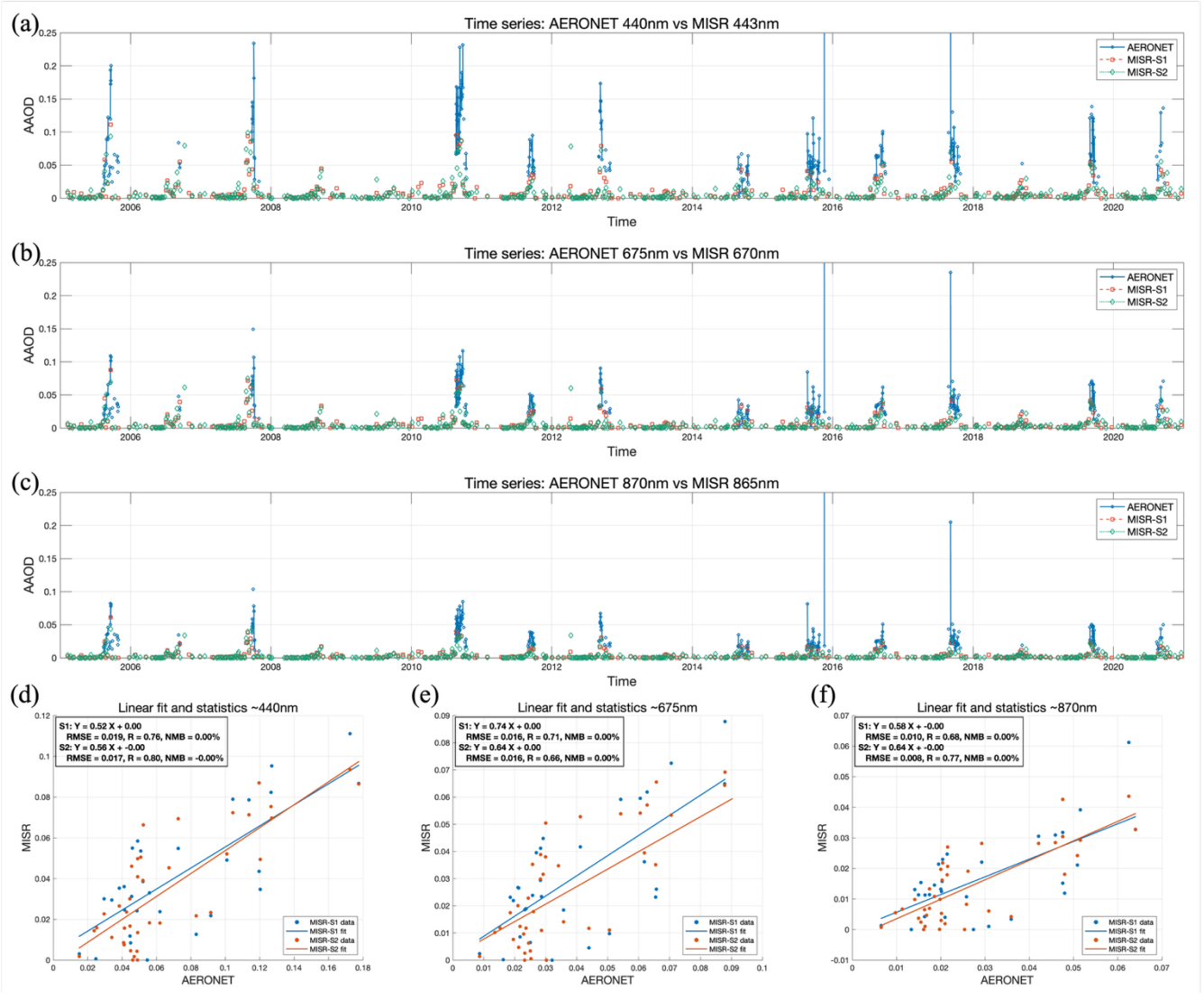

Figure B1. Time series analysis of AERONET CUIABA-MIRANDA site observations (2005–2020) and nearby MISR grid data at different spectral bands, and correlation analysis with outliers removed. (a) AAOD at ~440 nm time series. (b) AAOD at ~675 nm time series. (c) AAOD at ~870 nm time series. (d) AAOD at ~440 nm correlation analysis (outliers removed). (e) AAOD at ~675 nm correlation analysis (outliers removed). (f) AAOD at ~870 nm correlation analysis (outliers removed).

https://doi.org/10.5194/essd-2025-593
Preprint. Discussion started: 7 October 2025

Open Access Earth System Science Data Discussions

640 **Table C1. Annual average of BC atmospheric column num concentration in 9 regions from 2005 to 2020.**

BC NUM	NA1	SA2	E3	A4	EA5	SEA6	SA7	NA8	O9
2005	11224	8350	4449	8275	4570	6040	5408	2548	3064
2006	12391	8465	4664	8241	4999	6488	5862	3096	3478
2007	12024	10418	4556	7288	4753	6464	5603	2622	4426
2008	12155	7712	4112	7860	5381	6380	6269	2941	3125
2009	11126	7319	4573	7943	4854	7159	6940	2536	3515
2010	12250	9642	4439	8191	5122	5865	5989	2907	3172
2011	11367	8246	4203	8058	4338	6303	5906	2590	5858
2012	10864	9521	4295	8155	4741	6165	6210	2843	4951
2013	10944	7947	4494	8227	4899	5949	6037	2746	3107
2014	11896	7854	4312	7391	4668	5991	5686	2700	3625
2015	10962	7473	4557	7964	4641	5816	5978	2794	3209
2016	12252	8552	4988	8087	4675	5057	6122	2659	3047
2017	11397	8062	5090	8245	4408	5266	6005	2957	4254
2018	10194	7495	4398	7911	4657	5485	7198	2650	3369
2019	11053	9037	3952	7558	4157	5706	6020	2533	3277
2020	13167	9259	4966	7793	4224	5300	6446	2630	2977

Table C2. Annual average of BC core size in 9 regions from 2005 to 2020.

BC MASS	NA1	SA2	E3	A4	EA5	SEA6	SA7	NA8	O9
2005	11224	8350	4449	8275	4570	6040	5408	2548	3064
2006	12391	8465	4664	8241	4999	6488	5862	3096	3478
2007	12024	10418	4556	7288	4753	6464	5603	2622	4426
2008	12155	7712	4112	7860	5381	6380	6269	2941	3125
2009	11126	7319	4573	7943	4854	7159	6940	2536	3515
2010	12250	9642	4439	8191	5122	5865	5989	2907	3172
2011	11367	8246	4203	8058	4338	6303	5906	2590	5858
2012	10864	9521	4295	8155	4741	6165	6210	2843	4951
2013	10944	7947	4494	8227	4899	5949	6037	2746	3107
2014	11896	7854	4312	7391	4668	5991	5686	2700	3625
2015	10962	7473	4557	7964	4641	5816	5978	2794	3209
2016	12252	8552	4988	8087	4675	5057	6122	2659	3047
2017	11397	8062	5090	8245	4408	5266	6005	2957	4254
2018	10194	7495	4398	7911	4657	5485	7198	2650	3369
2019	11053	9037	3952	7558	4157	5706	6020	2533	3277

https://doi.org/10.5194/essd-2025-593
Preprint. Discussion started: 7 October 2025

2020	13167	9259	4966	7793	4224	5300	6446	2630	2977

Table C3. Annual average of BC shell size in 9 regions from 2005 to 2020.

BC MASS	NA1	SA2	E3	A4	EA5	SEA6	SA7	NA8	O9
2005	11224	8350	4449	8275	4570	6040	5408	2548	3064
2006	12391	8465	4664	8241	4999	6488	5862	3096	3478
2007	12024	10418	4556	7288	4753	6464	5603	2622	4426
2008	12155	7712	4112	7860	5381	6380	6269	2941	3125
2009	11126	7319	4573	7943	4854	7159	6940	2536	3515
2010	12250	9642	4439	8191	5122	5865	5989	2907	3172
2011	11367	8246	4203	8058	4338	6303	5906	2590	5858
2012	10864	9521	4295	8155	4741	6165	6210	2843	4951
2013	10944	7947	4494	8227	4899	5949	6037	2746	3107
2014	11896	7854	4312	7391	4668	5991	5686	2700	3625
2015	10962	7473	4557	7964	4641	5816	5978	2794	3209
2016	12252	8552	4988	8087	4675	5057	6122	2659	3047
2017	11397	8062	5090	8245	4408	5266	6005	2957	4254
2018	10194	7495	4398	7911	4657	5485	7198	2650	3369
2019	11053	9037	3952	7558	4157	5706	6020	2533	3277
2020	13167	9259	4966	7793	4224	5300	6446	2630	2977

645

https://doi.org/10.5194/essd-2025-593
Preprint. Discussion started: 7 October 2025

References

Bergstrom, R. W., Pilewskie, P., Russell, P. B., Redemann, J., Bond, T. C., Quinn, P. K., and Sierau, B.: Spectral absorption properties of atmospheric aerosols, Atmos. Chem. Phys., 2007.

Bigi, A., Veratti, G., Andrews, E., Collaud Coen, M., Guerrieri, L., Bernardoni, V., Massabò, D., Ferrero, L., Teggi, S., and Ghermandi, G.: Aerosol absorption using in situ filter-based photometers and ground-based sun photometry in the Po Valley urban atmosphere, Atmos. Chem. Phys., 23, 14841–14869, https://doi.org/10.5194/acp-23-14841-2023, 2023.

Bond, T. C., Doherty, S. J., Fahey, D. W., Forster, P. M., Berntsen, T., DeAngelo, B. J., Flanner, M. G., Ghan, S., Kärcher, B., Koch, D., Kinne, S., Kondo, Y., Quinn, P. K., Sarofim, M. C., Schultz, M. G., Schulz, M., Venkataraman, C., Zhang, H., Zhang, S., Bellouin, N., Guttikunda, S. K., Hopke, P. K., Jacobson, M. Z., Kaiser, J. W., Klimont, Z., Lohmann, U., Schwarz, J. P., Shindell, D., Storelvmo, T., Warren, S. G., and Zender, C. S.: Bounding the role of black carbon in the climate system: A scientific assessment, JGR Atmospheres, 118, 5380–5552, https://doi.org/10.1002/jgrd.50171, 2013.

Bousserez, N., Guerrette, J. J., and Henze, D. K.: Enhanced parallelization of the incremental 4D-Var data assimilation algorithm using the Randomized Incremental Optimal Technique, Quart J Royal Meteoro Soc, 146, 1351–1371, https://doi.org/10.1002/qj.3740, 2020.

Cappa, C. D., Onasch, T. B., Massoli, P., Worsnop, D. R., Bates, T. S., Cross, E. S., Davidovits, P., Hakala, J., Hayden, K. L., Jobson, B. T., Kolesar, K. R., Lack, D. A., Lerner, B. M., Li, S.-M., Mellon, D., Nuaaman, I., Olfert, J. S., Petäjä, T., Quinn, P. K., Song, C., Subramanian, R., Williams, E. J., and Zaveri, R. A.: Radiative Absorption Enhancements Due to the Mixing State of Atmospheric Black Carbon, Science, 337, 1078–1081, https://doi.org/10.1126/science.1223447, 2012.

Cassee, F. R., Héroux, M.-E., Gerlofs-Nijland, M. E., and Kelly, F. J.: Particulate matter beyond mass: recent health evidence on the role of fractions, chemical constituents and sources of emission, Inhalation Toxicology, 25, 802–812, https://doi.org/10.3109/08958378.2013.850127, 2013.

Chakraborty, S., Devnath, M. K., Jabeli, A., Kulkarni, C., Boteju, G., Wang, J., and Janeja, V. P.: Impact of increased anthropogenic Amazon wildfires on Antarctic Sea ice melt via albedo reduction, Environ. Data Science, 4, e18, https://doi.org/10.1017/eds.2025.1, 2025.

Chathurangika, N. P. M., Haque, Md. M., Nyasulu, M., Khan, R., Ahmmad, N., Sheikh, M. A. A., Hossain, M. L., and Rahman, A. K. M. L.: Long-term trends in aerosol optical properties and their relationship with cloud properties over southern India and Sri Lanka, Intl Journal of Climatology, 42, 9051–9071, https://doi.org/10.1002/joc.7799, 2022.

Chen, B., Andersson, A., Lee, M., Kirillova, E. N., Xiao, Q., Kruså, M., Shi, M., Hu, K., Lu, Z., Streets, D. G., Du, K., and Gustafsson, Ö.: Source Forensics of Black Carbon Aerosols from China, Environ. Sci. Technol., 47, 9102–9108, https://doi.org/10.1021/es401599r, 2013.

Chen, Y. and Prinn, R. G.: Estimation of atmospheric methane emissions between 1996 and 2001 using a three-dimensional global chemical transport model, J. Geophys. Res., 111, 2005JD006058, https://doi.org/10.1029/2005JD006058, 2006.

Chung, C. E., Lee, K., and Müller, D.: Effect of internal mixture on black carbon radiative forcing, Tellus B: Chemical and Physical Meteorology, 64, 10925, https://doi.org/10.3402/tellusb.v64i0.10925, 2012.

Cohen, J. B.: Quantifying the occurrence and magnitude of the Southeast Asian fire climatology, Environ. Res. Lett., 9, 114018, https://doi.org/10.1088/1748-9326/9/11/114018, 2014.

https://doi.org/10.5194/essd-2025-593
Preprint. Discussion started: 7 October 2025

Cohen, J. B. and Wang, C.: Estimating global black carbon emissions using a top-down Kalman Filter approach, JGR Atmospheres, 119, 307–323, https://doi.org/10.1002/2013JD019912, 2014.

Cohen, J. B., Prinn, R. G., and Wang, C.: The impact of detailed urban-scale processing on the composition, distribution, and radiative forcing of anthropogenic aerosols: THE IMPACT OF DETAILED URBAN-SCALE PROCESSING, Geophys. Res. Lett., 38, n/a-n/a, https://doi.org/10.1029/2011GL047417, 2011.

Ding, A. J., Huang, X., Nie, W., Sun, J. N., Kerminen, V. -M., Petäjä, T., Su, H., Cheng, Y. F., Yang, X. -Q., Wang, M. H., Chi, X. G., Wang, J. P., Virkkula, A., Guo, W. D., Yuan, J., Wang, S. Y., Zhang, R. J., Wu, Y. F., Song, Y., Zhu, T., Zilitinkevich, S., Kulmala, M., and Fu, C. B.: Enhanced haze pollution by black carbon in megacities in China, Geophysical Research Letters, 43, 2873–2879, https://doi.org/10.1002/2016GL067745, 2016.

Freire, J. L. M., Longo, K. M., Freitas, S. R., Coelho, C. A. S., Molod, A. M., Marshak, J., Da Silva, A., and Ribeiro, B. Z.: To What Extent Biomass Burning Aerosols Impact South America Seasonal Climate Predictions?, Geophysical Research Letters, 47, e2020GL088096, https://doi.org/10.1029/2020GL088096, 2020.

Guo, J., Li, Y., Cohen, J. B., Li, J., Chen, D., Xu, H., Liu, L., Yin, J., Hu, K., and Zhai, P.: Shift in the Temporal Trend of Boundary Layer Height in China Using Long-Term (1979–2016) Radiosonde Data, Geophysical Research Letters, 46, 6080–6089, https://doi.org/10.1029/2019GL082666, 2019.

Hansen, J., Sato, M., Ruedy, R., Kharecha, P., Lacis, A., Miller, R., Nazarenko, L., Lo, K., Schmidt, G. A., Russell, G., Aleinov, I., Bauer, S., Baum, E., Cairns, B., Canuto, V., Chandler, M., Cheng, Y., Cohen, A., Del Genio, A., Faluvegi, G., Fleming, E., Friend, A., Hall, T., Jackman, C., Jonas, J., Kelley, M., Kiang, N. Y., Koch, D., Labow, G., Lerner, J., Menon, S., Novakov, T., Oinas, V., Perlwitz, Ja., Perlwitz, Ju., Rind, D., Romanou, A., Schmunk, R., Shindell, D., Stone, P., Sun, S., Streets, D., Tausnev, N., Thresher, D., Unger, N., Yao, M., and Zhang, S.: Climate simulations for 1880–2003 with GISS modelE, Clim Dyn, 29, 661–696, https://doi.org/10.1007/s00382-007-0255-8, 2007.

He, C., Liou, K.-N., Takano, Y., Zhang, R., Levy Zamora, M., Yang, P., Li, Q., and Leung, L. R.: Variation of the radiative properties during black carbon aging: theoretical and experimental intercomparison, Atmos. Chem. Phys., 15, 11967–11980, https://doi.org/10.5194/acp-15-11967-2015, 2015.

Helin, A., Virkkula, A., Backman, J., Pirjola, L., Sippula, O., Aakko-Saksa, P., Väätäinen, S., Mylläri, F., Järvinen, A., Bloss, M., Aurela, M., Jakobi, G., Karjalainen, P., Zimmermann, R., Jokiniemi, J., Saarikoski, S., Tissari, J., Rönkkö, T., Niemi, J. V., and Timonen, H.: Variation of Absorption Ångström Exponent in Aerosols From Different Emission Sources, JGR Atmospheres, 126, e2020JD034094, https://doi.org/10.1029/2020JD034094, 2021.

Hodnebrog, Ø., Myhre, G., and Samset, B. H.: How shorter black carbon lifetime alters its climate effect, Nat Commun, 5, 5065, https://doi.org/10.1038/ncomms6065, 2014.

Huang, K.-T., Sui, C.-H., Lo, M.-H., Kuo, Y.-Y., and Chang, C.-W. J.: Effects of anthropogenic aerosols on the evolution of Indian summer monsoon, Terr Atmos Ocean Sci, 34, 10, https://doi.org/10.1007/s44195-023-00041-7, 2023.

Jacobson, M. Z.: Strong radiative heating due to the mixing state of black carbon in atmospheric aerosols, Nature, 409, 695–697, https://doi.org/10.1038/35055518, 2001.

Jaganathan, S., Rajiva, A., Amini, H., De Bont, J., Dixit, S., Dutta, A., Kloog, I., Lane, K. J., Menon, J. S., Nori-Sarma, A., Prabhakaran, D., Schwartz, J., Sharma, P., Stafoggia, M., Walia, G. K., Wellenius, G. A., Prabhakaran, P., Ljungman, P., and Mandal, S.: Nationwide analysis of air pollution hotspots across India: A spatiotemporal PM2.5 trend analysis (2008–2019), Environmental Research, 264, 120276, https://doi.org/10.1016/j.envres.2024.120276, 2025.

https://doi.org/10.5194/essd-2025-593
Preprint. Discussion started: 7 October 2025

Junghenn Noyes, K. T., Kahn, R. A., Limbacher, J. A., and Li, Z.: Canadian and Alaskan wildfire smoke particle properties, their evolution, and controlling factors, from satellite observations, Atmos. Chem. Phys., 22, 10267–10290, https://doi.org/10.5194/acp-22-10267-2022, 2022.

Kawano, A., Kelp, M., Qiu, M., Singh, K., Chaturvedi, E., Dahiya, S., Azevedo, I., and Burke, M.: Improved daily PM2.5 estimates in India reveal inequalities in recent enhancement of air quality, Science AdvAnceS, 2025.

Kim, D., Wang, C., Ekman, A. M. L., Barth, M. C., and Rasch, P. J.: Distribution and direct radiative forcing of carbonaceous and sulfate aerosols in an interactive size-resolving aerosol–climate model, J. Geophys. Res., 113, 2007JD009756, https://doi.org/10.1029/2007JD009756, 2008.

Krol, M. C., Hooghiemstra, P. B., Van Leeuwen, T. T., Van Der Werf, G. R., Novelli, P. C., Deeter, M. N., Aben, I., and Röckmann, T.: Correction to "Interannual variability of carbon monoxide emission estimates over South America from 2006 to 2010," JGR Atmospheres, 118, 5061–5064, https://doi.org/10.1002/jgrd.50389, 2013.

Kumar, P., Beig, G., Singh, V., Sahu, S. K., Siingh, D., and Bamniya, B. R.: Model simulation of carbonaceous fine particulate matter using SAFAR emission inventory and comparison with EDGAR-HTAP simulations, Atmospheric Environment, 315, 120147, https://doi.org/10.1016/j.atmosenv.2023.120147, 2023.

Kunjir, G. M., Tikle, S., Das, S., Karim, M., Roy, S. K., and Chatterjee, U.: Assessing particulate matter (PM2.5) concentrations and variability across Maharashtra using satellite data and machine learning techniques, Discov Sustain, 6, 238, https://doi.org/10.1007/s43621-025-01082-3, 2025.

Lee, J., Yun, J., and Kim, K. J.: Monitoring of black carbon concentration at an inland rural area including fixed sources in Korea, Chemosphere, 143, 3–9, https://doi.org/10.1016/j.chemosphere.2015.04.003, 2016.

Li, B., Gasser, T., Ciais, P., Piao, S., Tao, S., Balkanski, Y., Hauglustaine, D., Boisier, J.-P., Chen, Z., Huang, M., Li, L. Z., Li, Y., Liu, H., Liu, J., Peng, S., Shen, Z., Sun, Z., Wang, R., Wang, T., Yin, G., Yin, Y., Zeng, H., Zeng, Z., and Zhou, F.: The contribution of China's emissions to global climate forcing, Nature, 531, 357–361, https://doi.org/10.1038/nature17165, 2016.

Li, J., Carlson, B. E., Yung, Y. L., Lv, D., Hansen, J., Penner, J. E., Liao, H., Ramaswamy, V., Kahn, R. A., Zhang, P., Dubovik, O., Ding, A., Lacis, A. A., Zhang, L., and Dong, Y.: Scattering and absorbing aerosols in the climate system, Nat Rev Earth Environ, 3, 363–379, https://doi.org/10.1038/s43017-022-00296-7, 2022a.

Li, L., Dubovik, O., Derimian, Y., Schuster, G. L., Lapyonok, T., Litvinov, P., Ducos, F., Fuertes, D., Chen, C., Li, Z., Lopatin, A., Torres, B., and Che, H.: Retrieval of aerosol components directly from satellite and ground-based measurements, Atmos. Chem. Phys., 19, 13409–13443, https://doi.org/10.5194/acp-19-13409-2019, 2019.

Li, L., Che, H., Derimian, Y., Dubovik, O., Schuster, G. L., Chen, C., Li, Q., Wang, Y., Guo, B., and Zhang, X.: Retrievals of fine mode light-absorbing carbonaceous aerosols from POLDER/PARASOL observations over East and South Asia, Remote Sensing of Environment, 247, 111913, https://doi.org/10.1016/j.rse.2020.111913, 2020.

Li, L., Derimian, Y., Chen, C., Zhang, X., Che, H., Schuster, G. L., Fuertes, D., Litvinov, P., Lapyonok, T., Lopatin, A., Matar, C., Ducos, F., Karol, Y., Torres, B., Gui, K., Zheng, Y., Liang, Y., Lei, Y., Zhu, J., Zhang, L., Zhong, J., Zhang, X., and Dubovik, O.: Climatology of aerosol component concentrations derived from multi-angular polarimetric POLDER-3 observations using GRASP algorithm, Earth Syst. Sci. Data, 14, 3439–3469, https://doi.org/10.5194/essd-14-3439-2022, 2022b.

Li, L., Che, H., Su, X., Zhang, X., Gui, K., Zheng, Y., Zhao, H., Zhao, H., Liang, Y., Lei, Y., Zhang, L., Zhong, J., Wang, Z., and Zhang, X.: Quantitative Evaluation of Dust and Black Carbon Column Concentration in the MERRA-2 Reanalysis Dataset Using Satellite-Based Component Retrievals, Remote Sensing, 15, 388, https://doi.org/10.3390/rs15020388, 2023.

Li, M., Zhang, Q., Kurokawa, J., Woo, J.-H., He, K., Lu, Z., Ohara, T., Song, Y., Streets, D. G., Carmichael, G. R., Cheng, Y., Hong, C., Huo, H., Jiang, X., Kang, S., Liu, F., Su, H., and Zheng, B.: MIX: a mosaic Asian anthropogenic emission inventory under the international collaboration framework of the MICS-Asia and HTAP, Atmos. Chem. Phys., 17, 935–963, https://doi.org/10.5194/acp-17-935-2017, 2017.

Li, X., Cohen, J. B., Tiwari, P., Wu, L., Wang, S., He, Q., Yang, H., and Qin, K.: Space-based inversion reveals underestimated carbon monoxide emissions over Shanxi, Commun Earth Environ, 6, 357, https://doi.org/10.1038/s43247-025-02301-5, 2025.

Limbacher, J. A., Kahn, R. A., and Lee, J.: The new MISR research aerosol retrieval algorithm: a multi-angle, multi-spectral, bounded-variable least squares retrieval of aerosol particle properties over both land and water, Atmos. Meas. Tech., 15, 6865–6887, https://doi.org/10.5194/amt-15-6865-2022, 2022.

Lin, C., Cohen, J. B., Wang, S., and Lan, R.: Application of a combined standard deviation and mean based approach to MOPITT CO column data, and resulting improved representation of biomass burning and urban air pollution sources, Remote Sensing of Environment, 241, 111720, https://doi.org/10.1016/j.rse.2020.111720, 2020.

Liu, J., Cohen, J. B., Tiwari, P., Liu, Z., Yim, S. H.-L., Gupta, P., and Qin, K.: New top-down estimation of daily mass and number column density of black carbon driven by OMI and AERONET observations, Remote Sensing of Environment, 315, 114436, https://doi.org/10.1016/j.rse.2024.114436, 2024a.

Liu, Z., Cohen, J. B., Wang, S., Wang, X., Tiwari, P., and Qin, K.: Remotely sensed BC columns over rapidly changing Western China show significant decreases in mass and inconsistent changes in number, size, and mixing properties due to policy actions, npj Clim Atmos Sci, 7, 124, https://doi.org/10.1038/s41612-024-00663-9, 2024b.

Liu, Z., Cohen, J. B., Tiwari, P., Guan, L., Wang, S., and Qin, K.: Data from "A Global Black Carbon Dataset of Column Concentration and Microphysical Information Derived from MISR Muti-band Observations and Mie Scattering Simulations" (2004.10.1–2020.12.31), figshare [dataset], https://doi.org/10.6084/m9.figshare.30173917, 2025.

Lu, L., Cohen, J. B., Qin, K., Li, X., and He, Q.: Identifying missing sources and reducing NO_x emissions uncertainty over China using daily satellite data and a mass-conserving method, Atmos. Chem. Phys., 25, 2291–2309, https://doi.org/10.5194/acp-25-2291-2025, 2025.

Lund, M. T., Berntsen, T. K., and Samset, B. H.: Sensitivity of black carbon concentrations and climate impact to aging and scavenging in OsloCTM2–M7, Atmos. Chem. Phys., 17, 6003–6022, https://doi.org/10.5194/acp-17-6003-2017, 2017.

Lund, M. T., Samset, B. H., Skeie, R. B., Watson-Parris, D., Katich, J. M., Schwarz, J. P., and Weinzierl, B.: Short Black Carbon lifetime inferred from a global set of aircraft observations, npj Clim Atmos Sci, 1, 31, https://doi.org/10.1038/s41612-018-0040-x, 2018.

Luo, B., Zhang, Y., Tang, T., Zhang, H., Hu, J., Mu, J., Wang, W., and Xue, L.: Spatial–temporal patterns in anthropogenic and biomass burning emission contributions to air pollution and mortality burden changes in India from 1995 to 2014, Atmos. Chem. Phys., 25, 4767–4783, https://doi.org/10.5194/acp-25-4767-2025, 2025.

Ma, Y., Ye, J., Xin, J., Zhang, W., Vilà-Guerau De Arellano, J., Wang, S., Zhao, D., Dai, L., Ma, Y., Wu, X., Xia, X., Tang, G., Wang, Y., Shen, P., Lei, Y., and Martin, S. T.: The Stove, Dome, and Umbrella Effects of Atmospheric Aerosol on the

https://doi.org/10.5194/essd-2025-593
Preprint. Discussion started: 7 October 2025

Development of the Planetary Boundary Layer in Hazy Regions, Geophysical Research Letters, 47, e2020GL087373, https://doi.org/10.1029/2020GL087373, 2020.

Mallet, M., Solmon, F., Roblou, L., Peers, F., Turquety, S., Waquet, F., Jethva, H., and Torres, O.: Simulation of Optical Properties and Direct and Indirect Radiative Effects of Smoke Aerosols Over Marine Stratocumulus Clouds During Summer 2008 in California With the Regional Climate Model RegCM, JGR Atmospheres, 122, https://doi.org/10.1002/2017JD026905, 2017.

Mylläri, F., Pirjola, L., Lihavainen, H., Asmi, E., Saukko, E., Laurila, T., Vakkari, V., O'Connor, E., Rautiainen, J., Häyrinen, A., Niemelä, V., Maunula, J., Hillamo, R., Keskinen, J., and Rönkkö, T.: Characteristics of particle emissions and their atmospheric dilution during co-combustion of coal and wood pellets in a large combined heat and power plant, Journal of the Air & Waste Management Association, 69, 97–108, https://doi.org/10.1080/10962247.2018.1521349, 2019.

Ramachandran, S., Ansari, K., and Cherian, R.: Air Pollution to Atmospheric Warming: Effects of Increasing Anthropogenic Aerosols on South Asia's Climate, Earth Syst Environ, https://doi.org/10.1007/s41748-025-00732-w, 2025.

Ramanathan, V. and Carmichael, G.: Global and regional climate changes due to black carbon, Nature Geosci, 1, 221–227, https://doi.org/10.1038/ngeo156, 2008.

Randles, C. A., Da Silva, A. M., Buchard, V., Colarco, P. R., Darmenov, A., Govindaraju, R., Smirnov, A., Holben, B., Ferrare, R., Hair, J., Shinozuka, Y., and Flynn, C. J.: The MERRA-2 Aerosol Reanalysis, 1980 Onward. Part I: System Description and Data Assimilation Evaluation, J. Climate, 30, 6823–6850, https://doi.org/10.1175/JCLI-D-16-0609.1, 2017.

Ren, Y., Oxford, C. R., Zhang, D., Liu, X., Zhu, H., Dillner, A. M., White, W. H., Chakrabarty, R. K., Hasheminassab, S., Diner, D. J., Le Roy, E. J., Kumar, J., Viteri, V., Song, K., Akoshile, C., Amador-Muñoz, O., Asfaw, A., Chang, R. Y.-W., Francis, D., Gahungu, P., Garland, R. M., Grutter, M., Kim, J., Langerman, K., Lee, P.-C., Lestari, P., Mayol-Bracero, O. L., Naidoo, M., Nelli, N., O'Neill, N., Park, S. S., Salam, A., Sarangi, B., Schechner, Y., Schofield, R., Tripathi, S. N., Windwer, E., Wu, M.-T., Zhang, Q., Rudich, Y., Brauer, M., and Martin, R. V.: Black carbon emissions generally underestimated in the global south as revealed by globally distributed measurements, Nat Commun, 16, 7010, https://doi.org/10.1038/s41467-025-62468-5, 2025.

Roberts, D. L. and Jones, A.: Climate sensitivity to black carbon aerosol from fossil fuel combustion, J. Geophys. Res., 109, 2004JD004676, https://doi.org/10.1029/2004JD004676, 2004.

Rosenfeld, D., Andreae, M. O., Asmi, A., Chin, M., De Leeuw, G., Donovan, D. P., Kahn, R., Kinne, S., Kivekäs, N., Kulmala, M., Lau, W., Schmidt, K. S., Suni, T., Wagner, T., Wild, M., and Quaas, J.: Global observations of aerosol-cloud-precipitation-climate interactions: Aerosol-cloud-climate interactions, Rev. Geophys., 52, 750–808, https://doi.org/10.1002/2013RG000441, 2014.

Russell, P. B., Bergstrom, R. W., Shinozuka, Y., Clarke, A. D., DeCarlo, P. F., Jimenez, J. L., Livingston, J. M., Redemann, J., Dubovik, O., and Strawa, A.: Absorption Angstrom Exponent in AERONET and related data as an indicator of aerosol composition, Atmos. Chem. Phys., 2010.

Santos, D. M. D., Oliveira, A. M. de, Duarte, E. S. F., Rodrigues, J. A., Menezes, L. S., Albuquerque, R., Roque, F. D. O., Peres, L. F., Hoelzemann, J. J., and Libonati, R.: Compound dry-hot-fire events connecting Central and Southeastern South America: an unapparent and deadly ripple effect, npj Nat. Hazards, 1, 32, https://doi.org/10.1038/s44304-024-00031-w, 2024.

Schutgens, N., Dubovik, O., Hasekamp, O., Torres, O., Jethva, H., Leonard, P. J. T., Litvinov, P., Redemann, J., Shinozuka, Y., De Leeuw, G., Kinne, S., Popp, T., Schulz, M., and Stier, P.: AEROCOM and AEROSAT AAOD and SSA study – Part

1: Evaluation and intercomparison of satellite measurements, Atmos. Chem. Phys., 21, 6895–6917, https://doi.org/10.5194/acp-21-6895-2021, 2021.

Schwarz, J. P., Spackman, J. R., Fahey, D. W., Gao, R. S., Lohmann, U., Stier, P., Watts, L. A., Thomson, D. S., Lack, D. A., Pfister, L., Mahoney, M. J., Baumgardner, D., Wilson, J. C., and Reeves, J. M.: Coatings and their enhancement of black carbon light absorption in the tropical atmosphere, J. Geophys. Res., 113, 2007JD009042, https://doi.org/10.1029/2007JD009042, 2008.

Senf, F., Heinold, B., Kubin, A., Müller, J., Schrödner, R., and Tegen, I.: How the extreme 2019–2020 Australian wildfires affected global circulation and adjustments, Atmos. Chem. Phys., 23, 8939–8958, https://doi.org/10.5194/acp-23-8939-2023, 2023.

Shaban, A., Kourtit, K., and Nijkamp, P.: Causality Between Urbanization and Economic Growth: Evidence From the Indian States, Front. Sustain. Cities, 4, 901346, https://doi.org/10.3389/frsc.2022.901346, 2022.

Shanmugam, K. R. and Odasseril, M. K.: India at 100 and the Significance of Top Six States, 2024.

Szidat, S., Jenk, T. M., Synal, H., Kalberer, M., Wacker, L., Hajdas, I., Kasper-Giebl, A., and Baltensperger, U.: Contributions of fossil fuel, biomass-burning, and biogenic emissions to carbonaceous aerosols in Zurich as traced by ^{14}C, J. Geophys. Res., 111, 2005JD006590, https://doi.org/10.1029/2005JD006590, 2006.

Tanaka, K., Berntsen, T., Fuglestvedt, J. S., and Rypdal, K.: Climate Effects of Emission Standards: The Case for Gasoline and Diesel Cars, Environ. Sci. Technol., 46, 5205–5213, https://doi.org/10.1021/es204190w, 2012.

Tegtmeier, S., Marandino, C., Jia, Y., Quack, B., and Mahajan, A. S.: Atmospheric gas-phase composition over the Indian Ocean, Atmos. Chem. Phys., 22, 6625–6676, https://doi.org/10.5194/acp-22-6625-2022, 2022.

Thornhill, G. D., Ryder, C. L., Highwood, E. J., Shaffrey, L. C., and Johnson, B. T.: The effect of South American biomass burning aerosol emissions on the regional climate, Atmos. Chem. Phys., 18, 5321–5342, https://doi.org/10.5194/acp-18-5321-2018, 2018.

Tiwari, P., Cohen, J. B., Wang, X., Wang, S., and Qin, K.: Radiative forcing bias calculation based on COSMO (Core-Shell Mie model Optimization) and AERONET data, npj Clim Atmos Sci, 6, 193, https://doi.org/10.1038/s41612-023-00520-1, 2023.

Tiwari, P., Cohen, J. B., Lu, L., Wang, S., Li, X., Guan, L., Liu, Z., Li, Z., and Qin, K.: Multi-platform observations and constraints reveal overlooked urban sources of black carbon in Xuzhou and Dhaka, Commun Earth Environ, 6, 38, https://doi.org/10.1038/s43247-025-02012-x, 2025.

Torres, O., Jethva, H., Ahn, C., Jaross, G., and Loyola, D. G.: TROPOMI aerosol products: evaluation and observations of synoptic-scale carbonaceous aerosol plumes during 2018–2020, Atmos. Meas. Tech., 13, 6789–6806, https://doi.org/10.5194/amt-13-6789-2020, 2020.

Wang, C., An, X., Hou, Q., Sun, Z., Li, Y., and Li, J.: Development of four-dimensional variational assimilation system based on the GRAPES–CUACE adjoint model (GRAPES–CUACE-4D-Var V1.0) and its application in emission inversion, Geosci. Model Dev., 14, 337–350, https://doi.org/10.5194/gmd-14-337-2021, 2021a.

Wang, H., Ding, J., Xu, J., Wen, J., Han, J., Wang, K., Shi, G., Feng, Y., Ivey, C. E., Wang, Y., Nenes, A., Zhao, Q., and Russell, A. G.: Aerosols in an arid environment: The role of aerosol water content, particulate acidity, precursors, and

relative humidity on secondary inorganic aerosols, Science of The Total Environment, 646, 564–572, https://doi.org/10.1016/j.scitotenv.2018.07.321, 2019.

Wang, S., Cohen, J. B., Lin, C., and Deng, W.: Constraining the relationships between aerosol height, aerosol optical depth and total column trace gas measurements using remote sensing and models, Atmos. Chem. Phys., 20, 15401–15426, https://doi.org/10.5194/acp-20-15401-2020, 2020.

Wang, S., Wang, X., Cohen, J. B., and Qin, K.: Inferring Polluted Asian Absorbing Aerosol Properties Using Decadal Scale AERONET Measurements and a MIE Model, Geophysical Research Letters, 48, e2021GL094300, https://doi.org/10.1029/2021GL094300, 2021b.

Wang, S., Cohen, J. B., Deng, W., Qin, K., and Guo, J.: Using a New Top-Down Constrained Emissions Inventory to Attribute the Previously Unknown Source of Extreme Aerosol Loadings Observed Annually in the Monsoon Asia Free Troposphere, Earth's Future, 9, e2021EF002167, https://doi.org/10.1029/2021EF002167, 2021c.

Wang, S., Cohen, J. B., Guan, L., Lu, L., Tiwari, P., and Qin, K.: Observationally constrained global NOx and CO emissions variability reveals sources which contribute significantly to CO2 emissions, npj Clim Atmos Sci, 8, 87, https://doi.org/10.1038/s41612-025-00977-2, 2025.

Wang, Z., Wang, Q., and Zhang, H.: Equilibrium climate response of the East Asian summer monsoon to forcing of anthropogenic aerosol species, J Meteorol Res, 31, 1018–1033, https://doi.org/10.1007/s13351-017-7059-5, 2017.

Wei, L., Lu, Z., Wang, Y., Liu, X., Wang, W., Wu, C., Zhao, X., Rahimi, S., Xia, W., and Jiang, Y.: Black carbon-climate interactions regulate dust burdens over India revealed during COVID-19, Nat Commun, 13, 1839, https://doi.org/10.1038/s41467-022-29468-1, 2022.

Xie, Y., Zeng, L., Hu, S., Wang, T., Du, Z., Tan, T., Xu, N., Chen, S., Mao, J., Xu, F., and Hu, M.: Long-term trends of black carbon levels, sources, and radiative effects from 2013 to 2022 in Beijing, China, npj Clean Air, 1, 10, https://doi.org/10.1038/s44407-025-00010-z, 2025.

Yang, J., Sakhvidi, M. J. Z., De Hoogh, K., Vienneau, D., Siemiatyck, J., Zins, M., Goldberg, M., Chen, J., Lequy, E., and Jacquemin, B.: Long-term exposure to black carbon and mortality: A 28-year follow-up of the GAZEL cohort, Environment International, 157, 106805, https://doi.org/10.1016/j.envint.2021.106805, 2021.

Yang, J., Kang, S., Chen, D., Zhao, L., Ji, Z., Duan, K., Deng, H., Tripathee, L., Du, W., Rai, M., Yan, F., Li, Y., and Gillies, R. R.: South Asian black carbon is threatening the water sustainability of the Asian Water Tower, Nat Commun, 13, 7360, https://doi.org/10.1038/s41467-022-35128-1, 2022.

Yu, H., Li, M., Zheng, X., Zhu, M., Zheng, Z., Xie, T., Yan, G., Hu, P., Cao, Z., Feng, J., and Sun, J.: Potential source and health risks of black carbon based on MERRA-2 reanalysis data in a typical industrial city of North China Plain, Journal of Environmental Management, 354, 120367, https://doi.org/10.1016/j.jenvman.2024.120367, 2024.

Zhang, Z., Li, J., Dong, Y., Zhang, C., Ying, T., and Li, Q.: Long-Term Trends in Aerosol Single Scattering Albedo Cause Bias in MODIS Aerosol Optical Depth Trends, IEEE Trans. Geosci. Remote Sensing, 62, 1–9, https://doi.org/10.1109/TGRS.2024.3424981, 2024.

Zhang, Z., Li, J., Che, H., Dong, Y., Dubovik, O., Eck, T., Gupta, P., Holben, B., Kim, J., Lind, E., Saud, T., Tripathi, S. N., and Ying, T.: Long-term trends in aerosol properties derived from AERONET measurements, Atmospheric Chemistry and Physics, 25, 4617–4637, https://doi.org/10.5194/egusphere-2024-2533, 2025.

https://doi.org/10.5194/essd-2025-593
Preprint. Discussion started: 7 October 2025

Zhao, C. and Garrett, T. J.: Effects of Arctic haze on surface cloud radiative forcing, Geophysical Research Letters, 42, 557–564, https://doi.org/10.1002/2014GL062015, 2015.

Zhao, C., Yang, Y., Chi, Y., Sun, Y., Zhao, X., Letu, H., and Xia, Y.: Recent progress in cloud physics and associated radiative effects in China from 2016 to 2022, Atmospheric Research, 293, 106899, https://doi.org/10.1016/j.atmosres.2023.106899, 2023.

Zhao, M., Dai, T., Goto, D., Wang, H., and Shi, G.: Assessing the assimilation of Himawari-8 observations on aerosol forecasts and radiative effects during pollution transport from South Asia to the Tibetan Plateau, Atmos. Chem. Phys., 24, 235–258, https://doi.org/10.5194/acp-24-235-2024, 2024.